

Digital micelles of encoded polymeric amphiphiles for direct sequence reading and ex vivo label-free quantification

Received: 30 March 2021

Accepted: 26 September 2022

Published online: 3 November 2022



Check for updates

**Qiangqiang Shi¹, Hao Yin², Rundi Song¹, Jie Xu¹, Jiajia Tan¹, Xin Zhou¹, Jie Cen¹,
Zhengyu Deng^{ID 1}, Huimin Tong³, Chenhui Cui⁴, Yanfeng Zhang⁴,
Xiaopeng Li^{ID 5}, Zhengbiao Zhang^{ID 6} and Shiyong Liu^{ID 1}**

Identification and quantification of synthetic polymers in complex biological milieu are crucial for delivery, sensing and scaffolding functions, but conventional techniques based on imaging probe labellings only afford qualitative results. Here we report modular construction of precise sequence-defined amphiphilic polymers that self-assemble into digital micelles with contour lengths strictly regulated by oligourethane sequences. Direct sequence reading is accomplished with matrix-assisted laser desorption/ionization (MALDI) tandem mass spectrometry, facilitated by high-affinity binding of alkali metal ions with poly(ethylene glycol) dendrons and selective cleavage of benzyl-carbamate linkages. A mixture of four types of digital micelles could be identified, sequence-decoded and quantified by MALDI and MALDI imaging at cellular, organ and tissue slice levels upon *in vivo* administration, enabling direct comparison of biological properties for each type of digital micelle in the same animal. The concept of digital micelles and encoded amphiphiles capable of direct sequencing and high-throughput label-free quantification could be exploited for next-generation precision nanomedicine designs (such as digital lipids) and protein corona studies.

Therapeutic and diagnostic systems based on nanoparticles (NPs) have been extensively investigated, and quite a few have now gained clinical approval¹. Ever-increasing types of NPs with distinct chemical, physical and biological characteristics are being fabricated, with the aim of controlling the biological fate of these NPs and overcoming multiple *in vivo* delivery barriers². Upon systemic (that is, intravenous) administration, the identification and spatiotemporal quantification

of NPs at the organ and tissue level are critical for understanding how the characteristics of NPs affect their movement and biodistribution^{3,4}. Compared to inorganic NPs, for which well-established characterization techniques (elemental/nuclear analysis) and intrinsic imaging methods (magnetic resonance and optical imaging, positron emission tomography) exist⁵, the *in vitro* and *in vivo* tracking of polymeric NPs—which represent the vast majority of nanomedicines currently

¹CAS Key Laboratory of Soft Matter Chemistry, Department of Polymer Science and Engineering, School of Chemistry and Materials Science, Collaborative Innovation Center of Chemistry for Energy Materials (iChEM), University of Science and Technology of China, Hefei, China. ²Mass Spectrometry Lab, Instruments Center for Physical Science, University of Science and Technology of China, Hefei, China. ³Center for Instrumental Analysis, Xi'an Jiaotong University, Xi'an, China. ⁴School of Chemistry, MOE Key Laboratory for Nonequilibrium Synthesis and Modulation of Condensed Matter, Xi'an Jiaotong University, Xi'an, China. ⁵College of Chemistry and Environmental Engineering, Shenzhen University, Shenzhen, China. ⁶State and Local Joint Engineering Laboratory for Novel Functional Polymeric Materials, College of Chemistry, Chemical Engineering and Materials Science, Soochow University, Suzhou, China. ✉e-mail: sliu@ustc.edu.cn

under clinical investigation and on the market—is generally more challenging due to the lack of suitable direct techniques⁶. Conventional fluorescent and isotopic labelling techniques⁵ might not provide the actual spatiotemporal distribution of polymeric NPs due to alteration of surface properties^{7,8}, inadvertent cleavage of conjugated labels⁹, background interference^{10,11} and spontaneous/triggered degradation¹². Thus, absolute quantification of the biodistribution of polymeric NPs remains a formidable challenge for nanomedicine design and assessment.

Another challenge in quantifying conventional polymeric NPs is due to their compositional heterogeneity, non-uniform chain lengths and lack of defined sequences compared to proteins, peptides and nucleic acids¹³. This situation has considerably changed with the advent of sequence-defined polymers with discrete molecular weights^{14–16}, and sequencing exploration by mass spectrometry (MS)^{17–21}. However, using either electrospray ionization (ESI) or matrix-assisted laser desorption/ionization (MALDI) sources, tandem MS characterization of precision polymers typically affords complex patterns, and sequence decoding requires the development of computer algorithms^{19,22,23}, limiting the applications of these methods in complex biological milieu²⁴. Meanwhile, hierarchical self-assembly of sequence-defined synthetic polymers into nanostructures and the effects of primary sequences on physical characteristics (size, shape, etc.) have remained unexplored^{25–27}. We envisage that nano-materials assembled from sequence-defined polymers possessing discrete molecular weights and an amphiphilic character could serve as model soft-matter nanocarriers for biodistribution quantification by MS if the following requirements were met: (1) appropriate mass range to bypass interference from abundant biological molecules; (2) high ionization efficiency to enable ideal MS detection sensitivity under both cellular and tissue conditions; and (3) facile identification, direct sequence readout and label-free quantification. Note that nanoassemblies of sequence-defined polymers carry built-in barcoded information^{28,29}. Thus, high-throughput and simultaneous quantification of NP mixtures by MS and tandem MS techniques could provide extra advantages compared to conventional fluorescence (qualitative with limited detection channels) and nuclear analysis (non-discernible decay among different nuclides) techniques. Moreover, sequence-defined polymers with discrete molecular weights are ideal analytes for MALDI-time of flight (TOF) MS identification and quantification^{23,30}, exhibiting tremendously enhanced signal intensities compared with conventional polymers with chain length dispersity.

Based on these criteria, we sought in this article to innovate digital micelles from precise amphiphiles containing a sequence-defined hydrophobic segment and a hydrophilic poly(ethylene glycol) (PEG) dendron (Fig. 1a). As designed, the PEG dendron not only endows the micelles with an amphiphilic character and self-assembling capability, but its intrinsic ionophilic nature³¹ enhances ionization efficiency and detection sensitivity under MALDI conditions. Furthermore, high-affinity binding of an alkali metal ion (Na^+) with a PEG dendron and selective cleavage of benzyl-carbamate covalent linkages synergistically contribute to clean tandem MS patterns (Fig. 1b). Remarkably, these sequence-encoded polymeric amphiphiles self-assemble into digital micelles with physical characteristics strictly regulated by primary sequences (Fig. 1c). We demonstrate high-throughput label-free quantification of cellular uptake extents, pharmacokinetics and biodistributions at both organ-extract and tissue-slice levels by MALDI-TOF MS and MALDI imaging for a mixture of four types of digital micelles in a single animal (Fig. 1d), providing direct comparison of corresponding *in vivo* biological behaviours on the same animal entities. In addition, the integration of a sequence-readable oligourethane segment with conventional small-molecule amphiphiles³² leads to ‘digital lipids’ and their applications as siRNA delivery nanocarriers and label-free cellular MS quantification were further explored.

Results and discussion

Rational design and modular synthesis of sequence-defined polymeric amphiphiles

Compared to ESI-MS, in which multiply charged species are overlaid and data interpretation is difficult, MALDI-TOF MS generates mostly singly charged species and affords cleaner MS patterns with excellent tolerance of contaminants and salts³⁰. However, during the decoding of sequence-defined polymers, MALDI tandem MS patterns can be still complicated by non-specific bond cleavages and by charged molecular fragments from both sides of each chain fragmentation event^{18,19,24,33,34}. Although the incorporation of labile linkages into polymers could enhance fragmentation selectivity, a delicate balance has to be ensured in our design to maintain the integrity of parent ions. Hence, we first aim to seek labile linkages with moderate bond strengths to ensure ion integrity under MALDI MS and achieve selective cleavage under tandem MS. Moreover, if we were able to manipulate the precise location (for example, at one terminal) of an alkali metal ion, subsequent tandem MS might only generate signals corresponding to molecular fragments bearing that alkali metal ion, whereas other fragments are uncharged and remain MS-invisible (Fig. 1).

Based on the above considerations, we start with polyurethanes possessing *N*-arylcarbamate repeating units (Fig. 2b). This type of polymer exhibits cascade or self-immolative depolymerization upon light-triggered unmasking of terminal aniline, which is strongly electron-donating ($\sigma_p^+ = -1.3$) and spontaneously activates the cleavage of neighbouring *N*-arylcarbamate, generating another terminal aniline moiety^{35–39}. We surmise that the weakly electron-donating *N*-carbamate ($\sigma_p^+ = -0.6$) might also partially stabilize the development of positive charge on the benzylic carbon atom and facilitate selective tandem MS fragmentation. Theoretical calculations of bond dissociation energies (BDEs) for model molecule 1 tend to support the above assumption (Fig. 2a). Benzyl-O linkages with the *N*-carbamate functionality at the *para* and *meta* positions exhibit BDEs of <50 kcal mol⁻¹ and ~70 kcal mol⁻¹, respectively, which are considerably lower than the BDEs of other covalent bonds within the model molecule and promising for further exploration. It is noteworthy that oligourethanes with benzyl-carbamate linkages, bearing no ester and amide bonds, are expected to be stable towards both hydrolytic and enzymatic degradation in complex biological milieu^{35,40}.

The synthesis of precise amphiphiles with sequence-defined polyurethane blocks relies on iterative cycles of coupling and deprotection steps (Fig. 2b). Starting from three monomeric units possessing aryl azide (AA) and *tert*-butyldimethylsilyl (TBS)-protected hydroxyl functionalities (AA-0-OTBS, AA-1-OTBS and AA-0'-OTBS; Supplementary Figs. 1–4), six types of encoded dimeric building blocks (AA-00-OTBS, AA-01-OTBS, AA-10-OTBS, AA-11-OTBS, AA-00'-OTBS and AA-0'0-OTBS) were initially constructed (Supplementary Schemes 1–6 and Supplementary Figs. 1–9). To endow sequence-defined polyurethanes with amphiphilic character, the synthesis of precisely encoded amphiphiles starts from a light-sensitive trigger (T) bearing a double-alkyl tail as both solubility enhancer and self-assembling promoter (Supplementary Scheme 7 and Supplementary Figs. 10 and 11), and terminates with a water-soluble PEG dendron (dPEG) possessing six triethylene glycol branches (Fig. 2b, Supplementary Scheme 8 and Supplementary Figs. 12 and 13). Dcation, the aryl azide moiety of the monomeric and dimeric building blocks undergoes Curtius rearrangement⁴¹ into aryl isocyanate upon heating and reacts *in situ* with terminal hydroxyl functionality; the crude product was then treated with *p*-toluenesulfonic acid for TBS deprotection (Fig. 2b). After reaching specified chain lengths for the polyurethane segment, the terminal hydroxyl moiety was capped with dPEG, affording precisely encoded polymeric amphiphiles with discrete molecular weights and predetermined sequences (Fig. 2c–f).

These sequence-defined polyurethanes and relevant encoded amphiphiles were thoroughly characterized by complementary

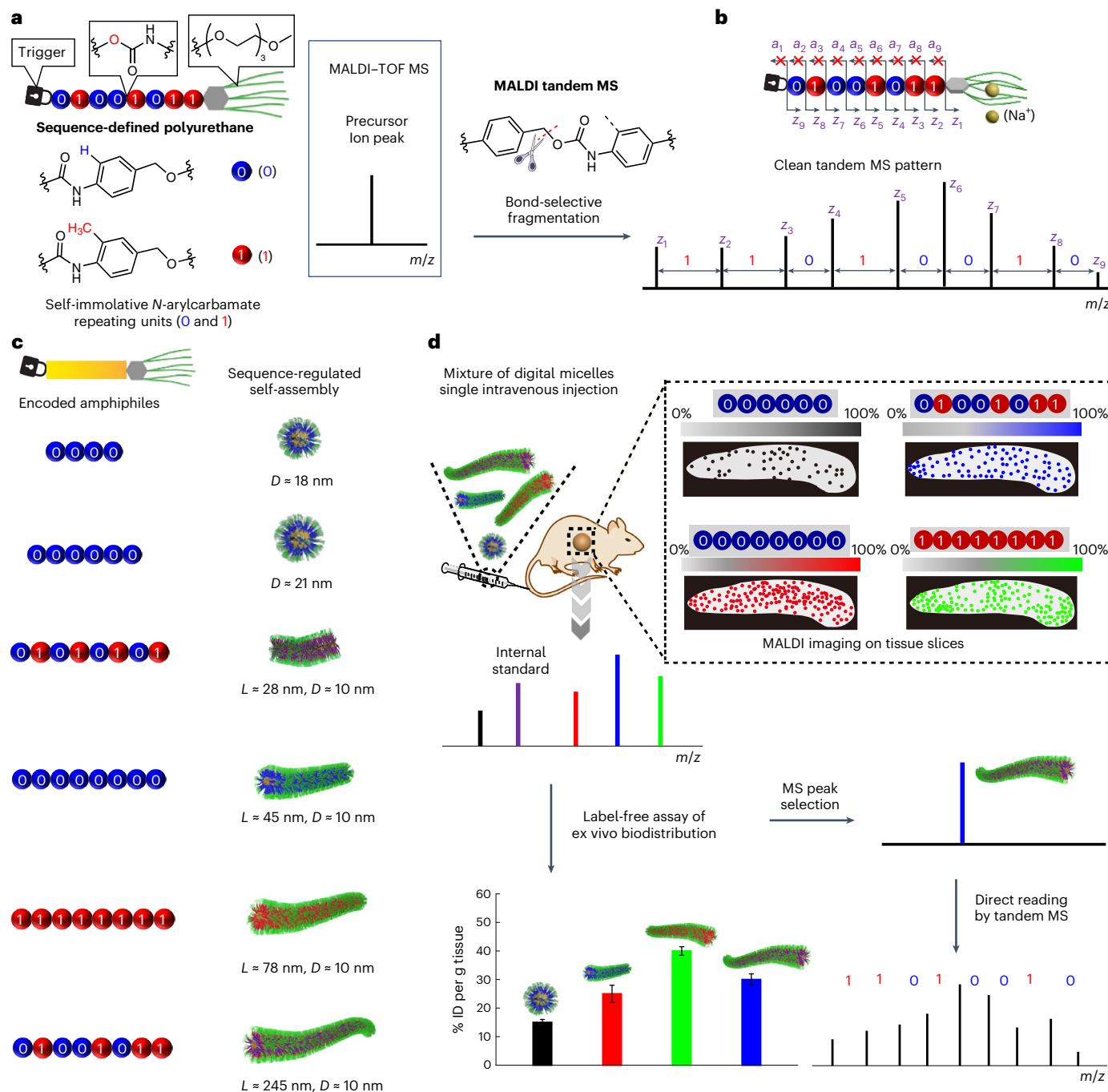


Fig. 1 | Direct sequence reading of encoded polymeric amphiphiles and sequence-regulated self-assembly into digital micelles for label-free ex vivo quantification. **a**, Schematics of sequence-defined polymeric amphiphiles consisting of a terminal trigger with a double-alkyl tail, a PEG dendron and *N*-arylcaramate repeating units, and *N*-(2-methylphenyl)caramate (**0**, blue spheres) and *N*-(2-methylphenyl)caramate (**1**, red spheres) in the hydrophobic polyurethane backbone. **b**, Direct sequence reading of encoded amphiphiles via MALDI tandem MS (Bruker LIFT module). Both selective cleavage of benzyl-O linkages and preferential Na^+ ion association with the PEG dendron at the single chain level

contribute to the clean secondary MS pattern. Note that fragments a_1-a_9 are MS-invisible due to their non-ionized nature. **c**, Sequence-regulated self-assembly of encoded polymeric amphiphiles into digital micelles. **d**, Upon intravenous injection of a mixture of digital micelles with varying contour lengths into SD rats, pharmacokinetics and in vivo biodistributions at both organ and tissue slice levels are assayed via MALDI-TOF MS and MALDI imaging in a label-free manner. Note that the sequence-encoded nature enables facile identification and direct reading for each type of digital micelles.

techniques (Supplementary Schemes 9–17 and Supplementary Figs. 14–29). MALDI-TOF MS revealed the formation of monodisperse polyurethane oligomers with discrete molecular weights corresponding to target lengths and sequences (Fig. 2c,f). Gel-permeation

chromatography (GPC) analysis revealed symmetric elution peaks with narrow polydispersity ($M_w/M_n \approx 1.008$) (Fig. 2d). The ^1H NMR spectra recorded for polyurethanes exhibited characteristic resonance signals ascribed to carbamate protons (~9.6 ppm) and methylene protons of

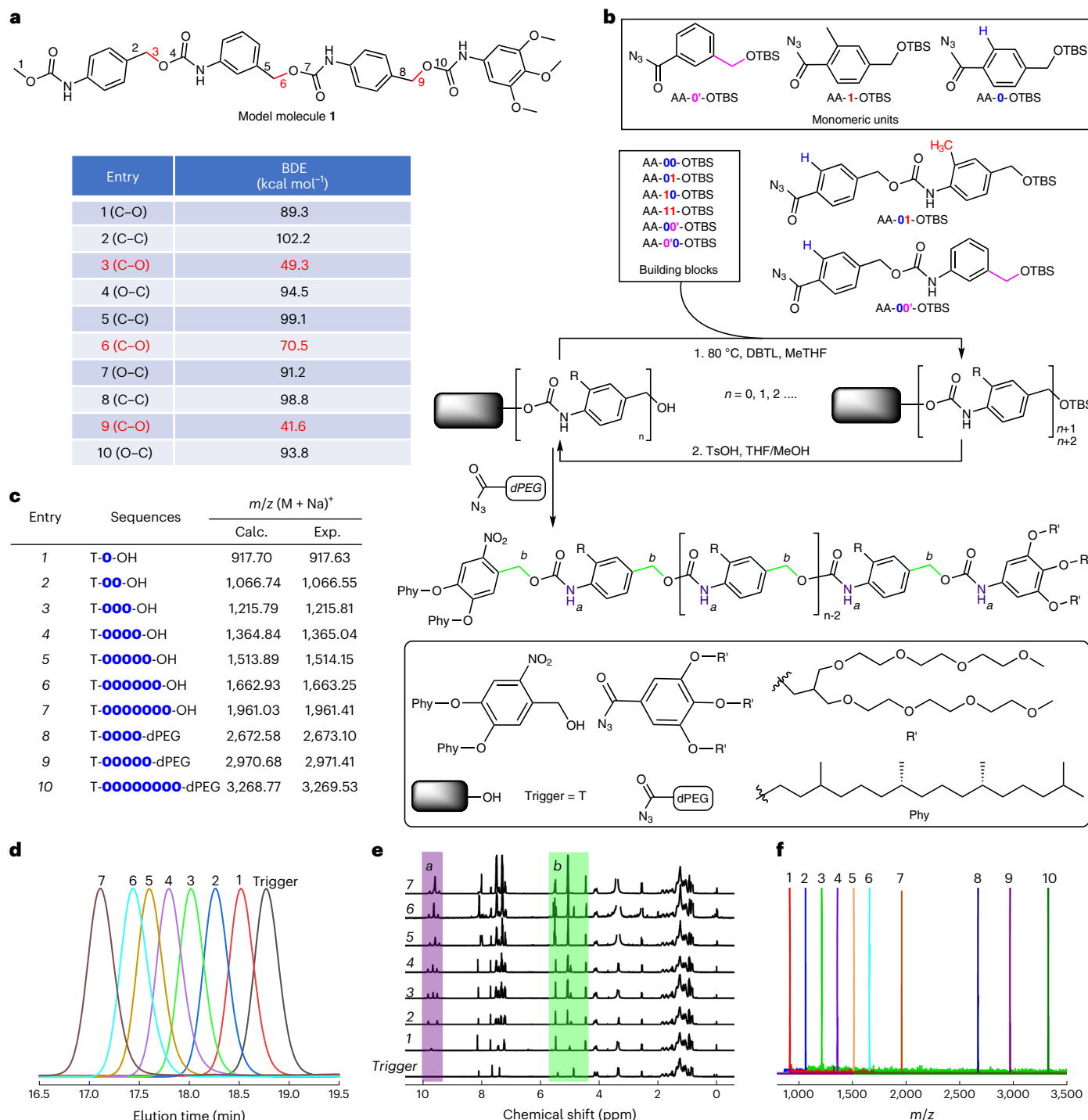


Fig. 2 | Modular synthesis of sequence-defined polyurethanes with uniform chain lengths. **a**, Calculation of BDEs of model molecule 1 (benzyl-O linkages with low BDEs are shown in red). **b**, Library of monomeric (**0**, **1**, **0'**) and dimeric (**00**, **11**, **01**, **10**, **00'**, **0'0**) building blocks possessing protected hydroxyl and aryl azide terminal functionalities; the latter undergo Curtius rearrangement into aryl isocyanate upon heating (80 °C) and efficiently react with the terminal hydroxyl moiety under catalysis of DBTL (1), followed by TBS deprotection actuated with TsOH (2); sequence-defined polyurethanes were modularly fabricated through iterative cycles of protocols (1) and (2). Note that the synthesis starts from a

light-sensitive trigger with a double-alkyl tail as both solubility enhancer and self-assembling promoter, and terminates with a hydrophilic dendron (dPEG). **c**, Summary of MALDI-TOF MS data of precise polyurethanes. **d–f**, THF GPC elution traces (**d**), ¹H NMR spectra (highlighted peaks in purple and green correspond to NH group labelled *a* and benzyl methylene groups labelled *b* in **b**, respectively) (**e**) and MALDI-TOF mass spectra (**f**) of sequence-defined polyurethanes and corresponding encoded polymeric amphiphiles. These GPC, NMR and MALDI data complementarily verified the successful synthesis of sequence-defined polymeric amphiphiles.

benzyl moieties (4.8–5.6 ppm; Fig. 2e). In addition, integrals of these resonance signals linearly increased upon chain extension, further verifying the molecular precision. Based on these established protocols,

a series of encoded amphiphiles bearing various sequence-defined polyurethane segments were modularly synthesized using **0**, **0'** and **1** as building blocks (Fig. 2b–f and Supplementary Figs. 14–29). Note that

0 and **1** only differ in the substituent (H versus CH₃) neighbouring the *N*-carbamate position. For model dimers and tetramers without and with the double-alkyl tail, CH₃-**11**-OH, T-**11**-OH and T-**1111**-OH possess the highest melting enthalpies (ΔH_s) compared with corresponding polyurethanes with uniform (**00**, **0000**) and alternating sequences (**01**, **0101**), with the latter exhibiting the lowest ΔH_s . These results revealed sequence-relevant distinct intrachain and interchain packing modes⁴² due to rotational restriction imposed by the methyl substituent towards the *N*-arylcaramate linkage (Supplementary Figs. 30 and 31 and Supplementary Table 1)⁴³.

ESI-MS was then used to characterize sequence-defined polymeric amphiphiles and examine the feasibility of bond cleavage selectivity (Supplementary Figs. 32–34). For T-**01001011**-dPEG with discrete molecular weights, the MS peak is associated with doubly charged ions, and ESI tandem MS reveals quite complicated patterns due to the presence of multiply charged species and irregular fragmentation pathways (Supplementary Fig. 33). A closer examination indicates that major fragmentation events occurred on benzyl-O linkages, verifying the labile nature (Fig. 2a). Upon fragmentation, z_n and a_n series of fragments corresponding to the PEG dendron side and the double-alkyl tail side, respectively, are clearly evident (Supplementary Fig. 33). Unfortunately, ESI tandem MS also generates molecular entities associated with multiple fragmentations (that is, b_n series) and uninterpretable tandem MS peaks, which are further complicated by overlaid multiply charged species (Supplementary Figs. 33 and 34). Note that this is typical for ESI tandem MS when applied in sequence decoding, causing considerable difficulties in MS data interpretation^{19–23,30}.

To circumvent iterative protection/deprotection steps, we further innovated an alternative strategy to construct sequence-defined polyurethanes by integrating two types of orthogonal isocyanate-generating chemistries (Fig. 3a): (1) tosylimino- λ^3 -iodane (PhINTs)-mediated Hofmann rearrangement of substituted arylamides into isocyanates⁴⁴; (2) Curtius rearrangement of aryl azides into isocyanates upon heating⁴¹. AA-**0**-OTBS and Am-**0**-OTBS were first synthesized to establish orthogonality and complementarity between these two processes (Supplementary Figs. 35 and 36). Next, a small library of monomeric and dimeric building blocks containing unprotected hydroxyl functionality was constructed (Fig. 3a and Supplementary Schemes 18 and 19). The ‘inverted’ synthesis of sequence-defined polyurethanes started from Phy₂AA bearing a double-alkyl tail and an aryl azide, and was terminated with the light-sensitive trigger NVOC in the final step. Specifically, Am-**00**-OH and AA-**00**-OH were utilized as building blocks to construct Phy₂-**000000**-NVOC via iterative protocols of orthogonal isocyanate generation and conjugation reactions (Fig. 3c,e, Supplementary Scheme 20 and Supplementary Figs. 37 and 38). Similarly, Phy₂-**100011**-NVOC was also modularly synthesized with molecular precision without the need for any protection/deprotection steps, demonstrating the modular nature of this synthesis, which is suitable for automation (Fig. 3d,e, Supplementary Scheme 21 and Supplementary Fig. 39).

Direct reading of encoded polymeric amphiphiles via MALDI tandem MS

Because the interpretation of ESI tandem MS data is not straightforward (Supplementary Figs. 32–34), we further attempted to use MALDI tandem MS for sequencing. As initially envisaged, clean MALDI tandem MS patterns with sequence-dictated neighbouring MS peak intervals were obtained, thus rendering facile and direct sequence reading (Fig. 1b). Taking T-**01001011**-dPEG as an example, the MALDI MS peak corresponds to a singly charged parent species, [M + Na]⁺ (Fig. 4a, left). When this precursor ion was selected and subjected to MALDI tandem MS in positive-ion mode (Supplementary Fig. 40), a clean tandem MS pattern was obtained, clearly revealing nine singly charged molecular fragments (z_1 – z_9 ; Fig. 4a, right).

When considering all possible fragmentation pathways, this series of tandem MS peaks are ascribed to molecular fragments bearing the same PEG dendron and one Na⁺ ion, with all fragmentation events occurring exclusively on benzyl-O linkages. Notably, following fragmentation, residual molecular fragments from the double-alkyl tail side, that is, a_n series, are completely invisible under tandem MS, which further contributes to the clean tandem MS pattern. Thus, the entire sequence information could be directly read from tandem MS peak intervals in the direction from high to low *m/z* ranges (Fig. 4a). MALDI tandem MS data of other encoded polymeric amphiphiles with a great variation in sequences all exhibited clean tandem MS patterns, enabling direct sequence readout (Supplementary Figs. 41–48). These results corroborate the universality of the current strategy for decoding sequence-defined polymeric amphiphiles. Compared to recent reports of utilizing ESI-MS and LC-MS to decode sequence-defined polymers based on cyclization-actuated cascade depolymerization in alkaline alcoholic media either at room temperature⁴⁵ or 70 °C (ref. ⁴⁶), which requires several hours to allow for self-immolative degradation, direct sequence reading using MALDI tandem MS offers considerable advantages.

In our design, the ionophilic PEG dendron (molecular weight, >1.3 kDa) facilitates the ionization process and enhances MALDI detection sensitivity, and prevents undesirable interference from the MALDI matrix and relevant heterogeneous impurities in the low *m/z* range. As a control, T-**00001111**-Phy, without a PEG dendron was synthesized (Supplementary Scheme 14 and Supplementary Fig. 24) and subjected to MALDI tandem MS analysis. Intriguingly, due to the loss of the preferential Na⁺ binding site, both a_n and the complementary z_n series of molecular fragments are clearly observed in tandem MS (Fig. 4b). In addition, MALDI tandem MS data of sequence-defined polyurethanes without a PEG dendron, T-**00000000**-OH, T-**01001011**-OH, T-**00001111**-OH, Phy₂-**000000**-NVOC and Phy₂-**100011**-NVOC, all reveal the presence of molecular fragments from both sides (a_n and complementary z_n series; Supplementary Figs. 49–53), and the experimental *m/z* values of each series accurately match with the calculated ones.

The extreme lability and selective fragmentation of benzyl-O linkages under MALDI tandem MS condition originate from the activation and electron-donating nature of *N*-carbamate functionality at the *para* position³⁵. Intriguingly, for T-**000'00000**-dPEG and T-**000000'00**-dPEG, MALDI tandem MS analysis reveals that the **0'** unit, in which the benzyl-O linkage is at the *meta* position relative to the *N*-carbamate moiety, remains intact and does not exhibit any tendency of tandem fragmentation under the same MALDI tandem MS condition (Extended Data Fig. 1 and Supplementary Fig. 54). These results are in agreement with the much higher BDE of the benzyl-O linkage in the **0'** unit (~70 kcal mol⁻¹) compared with that in the **0** unit (<50 kcal mol⁻¹; Fig. 2a). Compared with other benzyl-O linkages along the encoded chain, the benzyl-O linkage directly conjugated with trigger T (model molecule 2; Supplementary Fig. 55) also possesses a considerably higher BDE (~66.3 kcal mol⁻¹) due to the lack of activation by *N*-carbamate functionality at the *para* position, leading to a decreased fragmentation tendency and the lowest signal intensity for the tandem MS fragment with the highest *m/z* value (that is, the z_9 peak in Fig. 4a). These results also imply that the threshold BDE for selective covalent bond cleavage during MALDI tandem MS lies in the range of ~50–60 kcal mol⁻¹. Taken together, the above experimental and theoretical results provide solid evidence to support direct sequence reading of encoded polymeric amphiphiles from clean MALDI tandem MS patterns.

The capability of the ionophilic PEG dendron to boost MALDI detection sensitivity was further examined by directly performing MALDI MS characterization of the mixture of T-**000000**-dPEG and T-**000000**-OH (Supplementary Fig. 56). At a mass ratio and molar ratio of 1/1, the MS peak areas corresponding to T-**000000**-dPEG exhibit 7.6-fold and 9.0-fold increases compared with those of T-**000000**-OH,

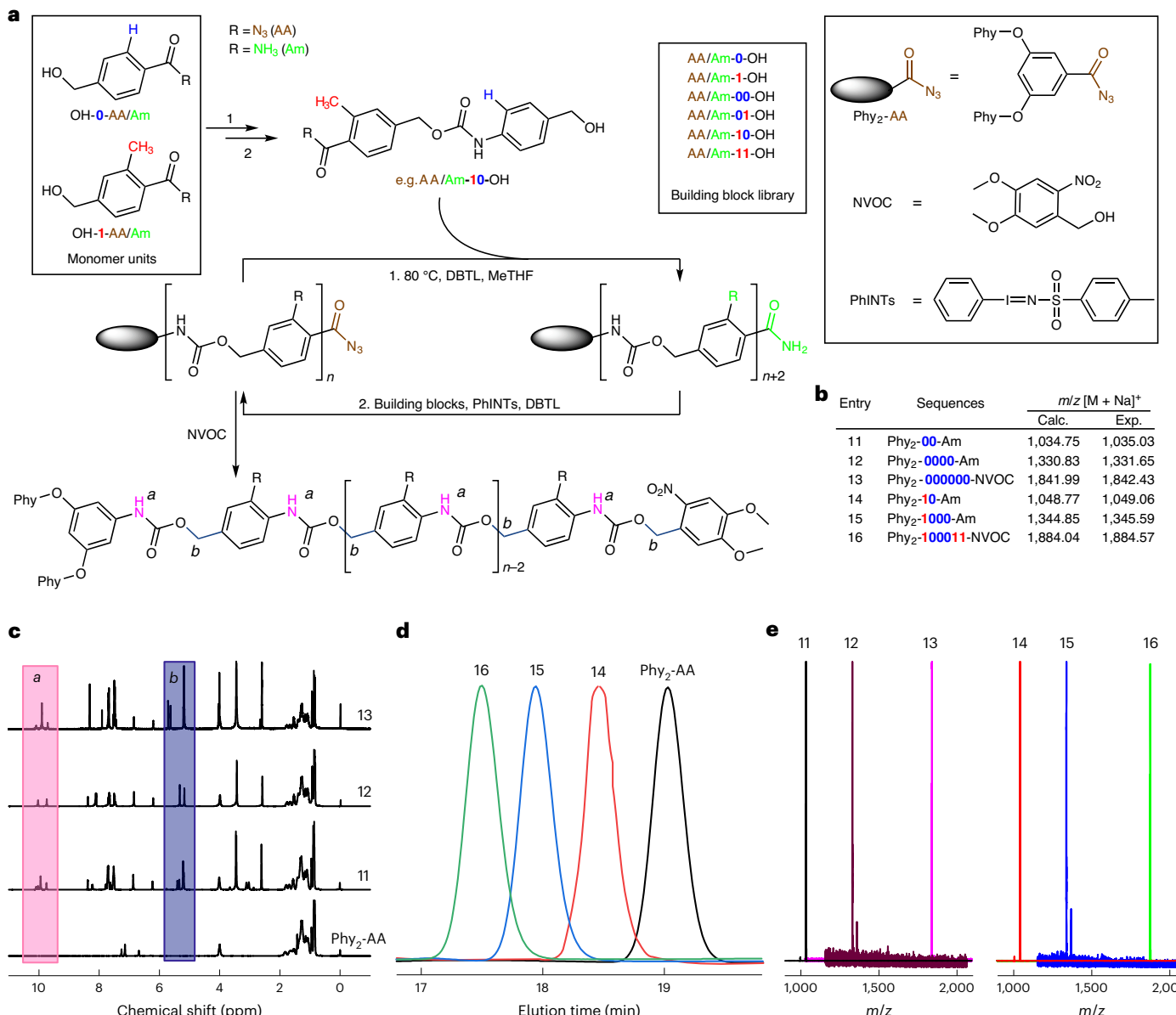


Fig. 3 | Facile synthesis of sequence-defined polyurethanes via orthogonal isocyanate-generating chemistries. **a**, Construction of monomeric and dimeric building blocks containing unprotected hydroxyl and either aryl azide (brown) or arylamide moieties (green). Aryl azide and arylamide functionalities in situ transform into aryl isocyanates (1) upon heating and treating with PhINTs at room temperature, respectively; newly generated isocyanate undergoes DBTL-catalysed addition reaction with hydroxyl of another building block bearing orthogonal isocyanate-generating moieties (2). Starting from the Phy₂-AA-bearing

double-phytane tail as solubility enhancer, iterative cycles of protocols (1) and (2) lead to sequence-defined polyurethanes with a light-sensitive trigger (NVOC) conjugated at the chain terminal. **b**, MALDI-TOF MS data of precise polyurethanes (entries 11–16). **c–e**, ¹H NMR spectra (highlighted peaks in pink and deep blue correspond to the NH group labelled *a* and benzyl methylene groups labelled *b* in **a**, respectively) (**c**), THF GPC elution traces (**d**) and MALDI-TOF mass spectra (**e**) of corresponding sequence-defined polyurethanes. These GPC, NMR, and MALDI data demonstrate the modular nature of the ‘inverted’ synthetic strategy.

although the former has a considerably higher molecular weight (2.97 kDa versus 1.66 kDa). Note that for MALDI MS analysis, primary MS signal intensities decay rapidly with the molecular weights of synthetic polymers. The PEG dendron-boosted MALDI detection sensitivity augurs well for the quantification and imaging of these encoded polymeric amphiphiles in complex biological milieu.

Sequence-regulated self-assembly of encoded polymeric amphiphiles into digital micelles

Note that in contrast to peptide, protein and DNA self-assembly, solution self-assembly of precise sequence-defined synthetic polymers

has been far less explored^{25,26} and the impact of primary sequences on self-assembling behaviour remains to be elucidated. We envisage that the molecular precision⁴⁷ and length/sequence of oligourethane segments could together contribute to their hierarchical self-assembly in aqueous media into higher-order nanostructures, categorized as ‘digital micelles’ due to their barcoded, identifiable and sequence-readable features (Fig. 1c). Cryogenic-transmission electron microscopy (cryo-TEM) was utilized to characterize resultant nanoassemblies of encoded polymeric amphiphiles with varying oligourethane lengths and sequences. Both T-**0000**-dPEG and T-**000000**-dPEG self-assemble into fairly monodisperse spherical micelles (nanospheres) with

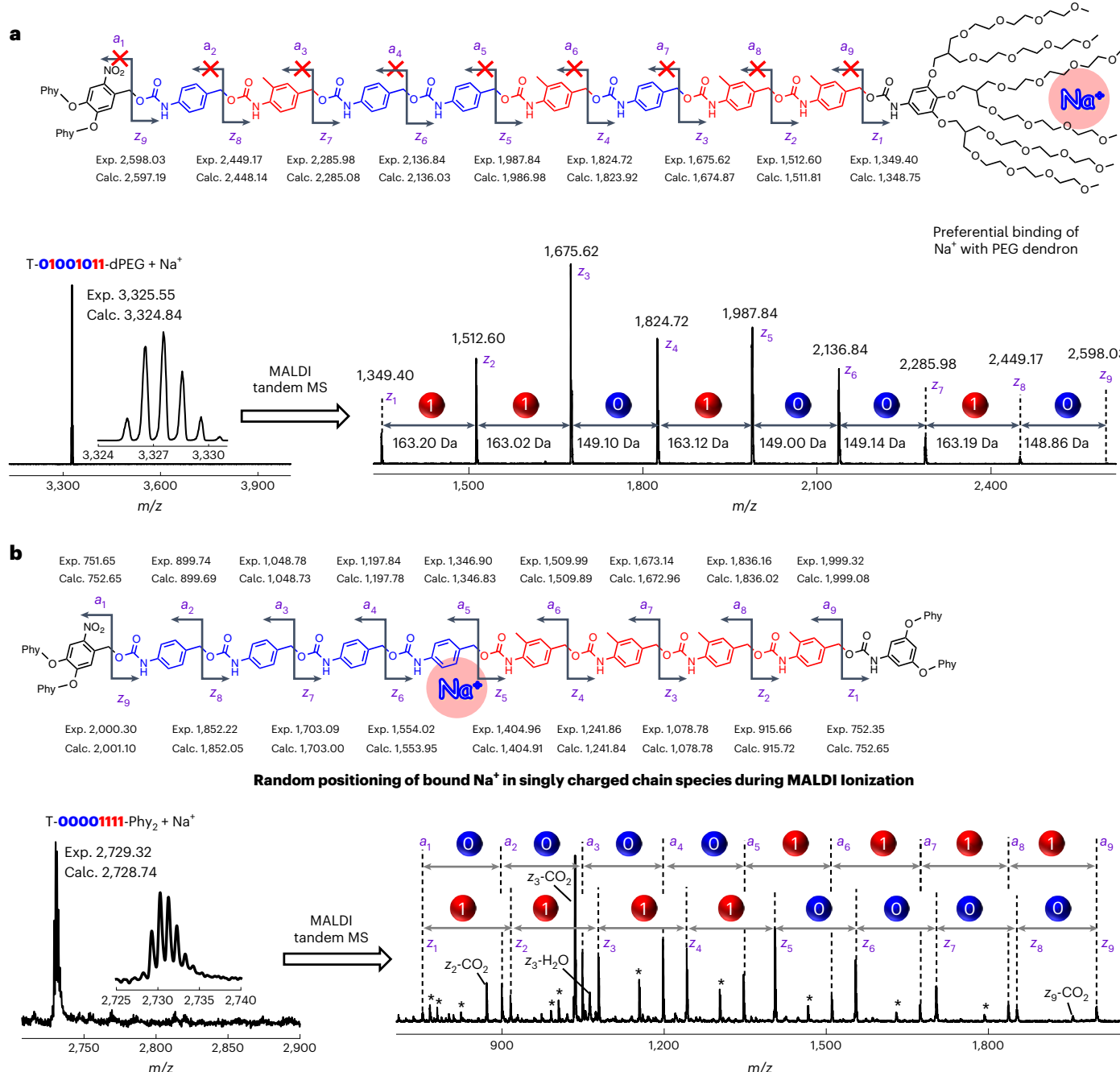


Fig. 4 | Direct reading of sequence-defined polyurethanes via MALDI tandem MS. **a**, MALDI–TOF MS and tandem MS (LIFT module) characterization of T-01001011-dPEG, together with MS peak assignments. The a_n series of fragments are completely absent under tandem MS due to preferential association of Na^+ .

ions with the PEG dendron at the single chain level. **b**, For T-00001111-Phy₂ under the MALDI tandem MS condition, both the a_n and z_n series of fragment peaks are clearly evident due to the absence of the ionophilic PEG dendron and loss of the preferential Na^+ binding mechanism. *Secondary fragmentation MS signals.

diameters, D , of ~ 18 nm and ~ 21 nm, respectively (Fig. 5a and Supplementary Fig. 57). Accordingly, small-angle X-ray scattering (SAXS) analysis of T-0000000-dPEG nanospheres afforded an overall diameter of ~ 18.2 nm from fitting with a spherical core–shell model (Supplementary Fig. 58a). For T-00000000-dPEG with an octameric polyurethane segment, short nanorods with uniform lengths ($L_n = 45.1$ nm, $L_w/L_n = 1.08$) were obtained via co-solvent-assisted self-assembly (Fig. 5c and Supplementary Fig. 59a,b), in which L_n and L_w are number-average and weight-average contour lengths, respectively. Fitting of the SAXS data of T-00000000-dPEG nanorods with a core–shell cylinder model revealed a core radius of ~ 4.0 nm, a shell thickness of ~ 1.8 nm and a

rod length of ~ 48.0 nm (Supplementary Fig. 58b). Such a transition from nanospheres to nanorods upon extending oligourethane length is consistent with the results of conventional amphiphilic block copolymers (BCPs) with varying hydrophobic/hydrophilic block ratios^{48,49}.

In contrast, T-11111111-dPEG with uniform repeating unit 1 self-assembles into longer nanorods with an L_n of 77.6 nm and an L_w/L_n of 1.04 (Fig. 5d and Supplementary Fig. 59c,d). The formation of longer nanorods for T-11111111-dPEG was further verified by both SAXS and dynamic light scattering (DLS) characterizations (Supplementary Fig. 58c and Supplementary Table 3). For T-01001011-dPEG with an irregular sequence, nanorods with more extended contour length

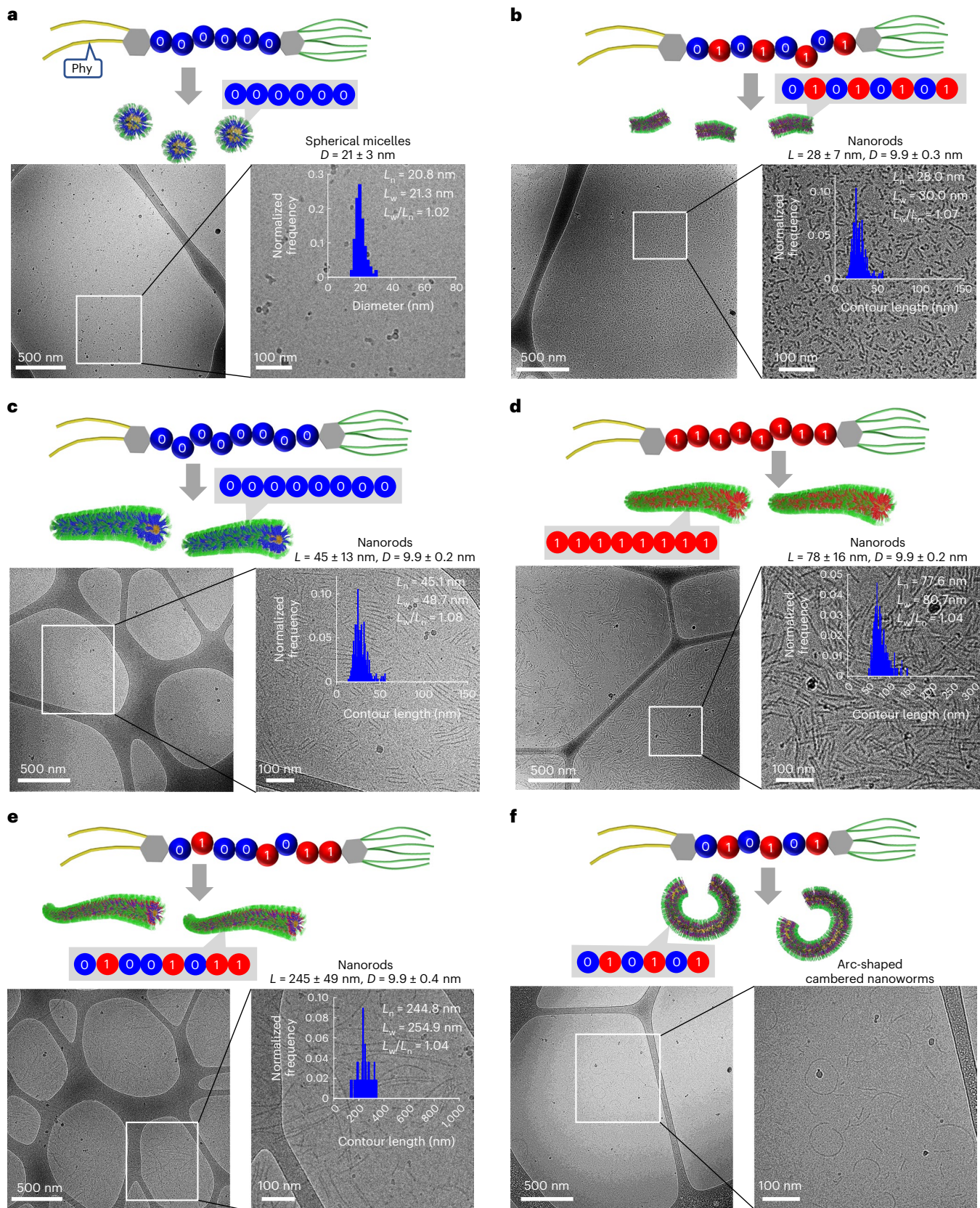


Fig. 5 | Sequence-regulated self-assembly of encoded polymeric amphiphiles into digital micelles with tunable contour lengths. **a–f**, Cryo-TEM images of nanostructures self-assembled from precise sequence-encoded amphiphilic polyurethanes in aqueous media: T-000000-dPEG (spherical micelles or nanospheres) (**a**), T-01010101-dPEG (ultrashort nanorods) (**b**), T-00000000-dPEG (short nanorods) (**c**), T-11111111-dPEG (longer nanorods) (**d**), T-01001011-dPEG (nanorods with more extended contour length) (**e**) and T-010101-dPEG (arc-shaped cambered nanoworms) (**f**). A transition from nanospheres to nanorods occurs upon extending oligourethane lengths and nanorod dimensions are regulated by oligourethane sequences. Cryo-TEM experiments were conducted at least three times for each sample, and the results are consistent and repeatable.

dPEG (nanorods with more extended contour length) (**e**) and T-010101-dPEG (arc-shaped cambered nanoworms) (**f**). A transition from nanospheres to nanorods occurs upon extending oligourethane lengths and nanorod dimensions are regulated by oligourethane sequences. Cryo-TEM experiments were conducted at least three times for each sample, and the results are consistent and repeatable.

($L_n = 244.8 \text{ nm}$, $L_w/L_n = 1.04$) could be obtained under the same conditions (Fig. 5e and Supplementary Fig. 60a,b), whereas the sequence isomer with the same total number of monomeric units **0** and **1**, T-**00001111**-dPEG, affords coexisting nanospheres and nanorods (Supplementary Fig. 61). When **0** and **1** are arranged in an alternating sequence, encoded polymeric amphiphiles T-**01010101**-dPEG and T-**010101**-dPEG exhibit distinct self-assembling morphologies. The former self-assembles into ultra-short nanorods with uniform contour lengths ($L_n = 28.0 \text{ nm}$, $L_w/L_n = 1.07$, $D \approx 9.9 \text{ nm}$; Fig. 5b and Supplementary Fig. 60c,d), whereas the latter affords unique arc-shaped, cambered nanoworms (Fig. 5f). Ultrashort nanorods of T-**01010101**-dPEG were further characterized by SAXS, revealing a core radius of $\sim 4.7 \text{ nm}$, a shell thickness of $\sim 1.6 \text{ nm}$ and a rod length of $\sim 30.3 \text{ nm}$ (Supplementary Fig. 58d).

As summarized in Fig. 6a, nanorods of encoded amphiphiles with octameric polyurethane segments and containing various sequences exhibit the same diameter ($\sim 10 \text{ nm}$) due to molecular precision, and have sequence-regulated dimensions with length polydispersities comparable to those achieved with crystallization-induced self-assembly^{48,50}. This is quite reasonable considering that these precise oligourethane segments are also highly crystalline (Supplementary Table 1 and Supplementary Fig. 31). Above a critical water content during the slow water addition process, initially formed aggregates could act as seeds for further growth into uniform nanorods. Sequence-regulated self-assembly and formation of arc-shaped cambered nanoworms could be ascribed to unique intrachain and inter-chain packing modes and crystalline lattice orientations dictated by oligourethane primary sequences^{42,51}. These results reveal the critical roles played by chain sequences and lengths in regulating solution self-assembly of precisely encoded amphiphiles.

We further examined the physicochemical properties and microstructural stability of digital micelles with encoded sequence information. A polarity-sensitive dye, Nile red, was used to assay micellar stability over the range of $0.0001\text{--}0.1 \mu\text{g ml}^{-1}$, and revealed critical micellization concentrations (CMCs) ranging from ~ 4.6 to $\sim 11.6 \mu\text{g ml}^{-1}$ (Supplementary Fig. 62 and Supplementary Table 2). These low CMC values, which decrease with increasing oligourethane length, could be ascribed to the C20 alkyl tail and crystalline oligourethane segment with cooperative hydrogen-bonding and $\pi\text{-}\pi$ interactions. For encoded polymeric amphiphiles with an octameric sequence, T-**11111111**-dPEG, which has the highest crystallization tendency (Supplementary Table 1), possesses the lowest CMC ($\sim 4.6 \mu\text{g ml}^{-1}$). Next, the Förster resonance energy transfer (FRET) technique was utilized to assess the stability of digital micelles against serum. A typical FRET pair, DiO and Dil, was coencapsulated into digital micelles and time-dependent evolutions of fluorescence spectra were recorded (Supplementary Figs. 63–65). Negligible changes of emission spectra and residual nanostructure fractions could be discerned upon coincubation in either PBS or 90% fetal bovine serum (FBS). The microstructural stability was further verified by direct cryo-TEM characterization (Supplementary Figs. 66–68).

To further elucidate the extent of micellar exchange between digital micelles, another FRET pair, NBD (donor, D) and MS735 (acceptor, A), was covalently conjugated onto the alkyl chain terminal of encoded amphiphiles, affording fluorophore-labelled polymeric amphiphiles NBD-2C12-**000000**-dPEG and MS735-2C12-**000000**-dPEG, respectively (Supplementary Schemes 22 and 23 and Supplementary Figs. 69–75). To probe micellar exchange between different types of digital micelles, M_D nanorods and M_A nanorods were coassembled from T-**01001011**-dPEG and NBD-2C12-**000000**-dPEG (95/5, wt/wt), and from T-**00000000**-dPEG and MS735-2C12-**000000**-dPEG (95/5, wt/wt), respectively (Supplementary Figs. 76 and 77). Upon mixing M_D and M_A nanorod dispersions (1/1, v/v), almost no change in fluorescence emission spectra was observed (Supplementary Fig. 78a,b), indicating that digital micelles are relatively ‘frozen’ and micellar exchange

essentially absent. Indeed, cryo-TEM results revealed a bimodal distribution of nanorods at 72 h after the mixing of short M_D nanorods and long M_A nanorods (Supplementary Fig. 78c). Taken together, these results conclusively verified the superior microstructural stability of digital micelles, auguring well for their biomedical applications.

Identification and label-free quantification of digital micelles at cellular levels

Compared to their spherical counterparts, elongated filaments self-assembled from amphiphilic BCPs were reported to possess extended blood circulation times¹², decreased extent of phagocytosis⁵² and less tendency to penetrate across the blood–brain barrier⁵³; however, the mechanisms and effects of nanorod lengths and diameters remain to be further elucidated⁵⁴. In addition, inconsistent results were obtained for cellular uptake tendencies of rod-like versus spherical polymeric nanoparticles due to variations in surface chemistry and stiffness^{55,56}. We propose that digital micelles with finely tuned contour lengths (28–245 nm) and narrow length distributions ($L_w/L_n < 1.08$; Fig. 5), could serve as an excellent model to investigate the shape effects of polymeric nanoparticles on biological behaviour by using MALDI–TOF MS as a label-free quantification tool (Fig. 1d). Furthermore, all digital micelles are densely coated with PEG dendrons (that is, have the same surface chemistry) and these encoded polymeric amphiphiles do not contain any amide or ester linkages. Thus, any hydrolytic/enzymatic degradation issues associated with polyester/polypeptide/DNA-based NPs can be safely avoided. The highly crystalline nature of their hydrophobic cores endows digital micelles with superior microstructural stability and mechanical robustness against shear forces and dilution effects upon in vivo administration.

As a prototype demonstration, we mixed four types of digital micelles self-assembled from T-**000000**-dPEG (nanospheres, $D \approx 21 \text{ nm}$), T-**00000000**-dPEG (nanorods; $L_n \approx 45 \text{ nm}$, $D \approx 10 \text{ nm}$), T-**11111111**-dPEG (nanorods; $L_n \approx 78 \text{ nm}$, $D \approx 10 \text{ nm}$) and T-**01001011**-dPEG (nanorods; $L_n \approx 245 \text{ nm}$, $D \approx 10 \text{ nm}$) for simultaneous label-free quantification by MALDI–TOF MS at cellular, organ and tissue slice levels (Extended Data Fig. 2a). Calibration curves for T-**000000**-dPEG, T-**00000000**-dPEG, T-**11111111**-dPEG and T-**01001011**-dPEG were readily acquired using T-**010101**-dPEG as the internal standard. Containing the same PEG dendron and double-alkyl tail and only differing in oligourethane sequences, the highly analogous nature of the encoded amphiphiles ensures MALDI reproducibility and quantification accuracy, as verified by established linear correlations (Extended Data Fig. 2b). The observed sequence-dependent slopes for MALDI calibration can be ascribed to different extents of crystallization tendency and non-covalent interactions with the *trans*-2-[3-(4-tert-butyl-phenyl)-2-methyl-2-propenylidene]malononitrile (DCTB) matrix, leading to varying MALDI ionization efficiencies. Indeed, T-**11111111**-dPEG exhibits the lowest MALDI calibration slope, which is in reasonable agreement with the highest melting enthalpies among a series of model tetramers (Supplementary Table 1) and the lowest CMC value among all types of digital micelles (Supplementary Table 2). Considering possible exchange between digital micelles and unimers under both in vitro and in vivo conditions, MALDI samples were fabricated in parallel from sequence-encoded amphiphiles in either unimer (THF solution) or micellar (aqueous dispersion) states over the concentration range of $0.05\text{--}15 \mu\text{g ml}^{-1}$. T-**00000000**-dPEG and T-**11111111**-dPEG exhibit MALDI detection sensitivities down to 0.5 and $1.0 \mu\text{g ml}^{-1}$, respectively (Extended Data Fig. 3a–d). Moreover, for a specific encoded polymeric amphiphile, MALDI signal intensities are almost independent of the initial state (unimers versus micelles). Note that comparable results were also obtained for T-**00000000**-dPEG and T-**11111111**-dPEG at the tissue slice level (Extended Data Fig. 3e,f).

We first investigated the cellular uptake tendencies of the mixture of digital micelles against both cancer cells (HepG2 and 4T1) and normal cells (LO2 and 3T3). At specified time intervals during coincubation,

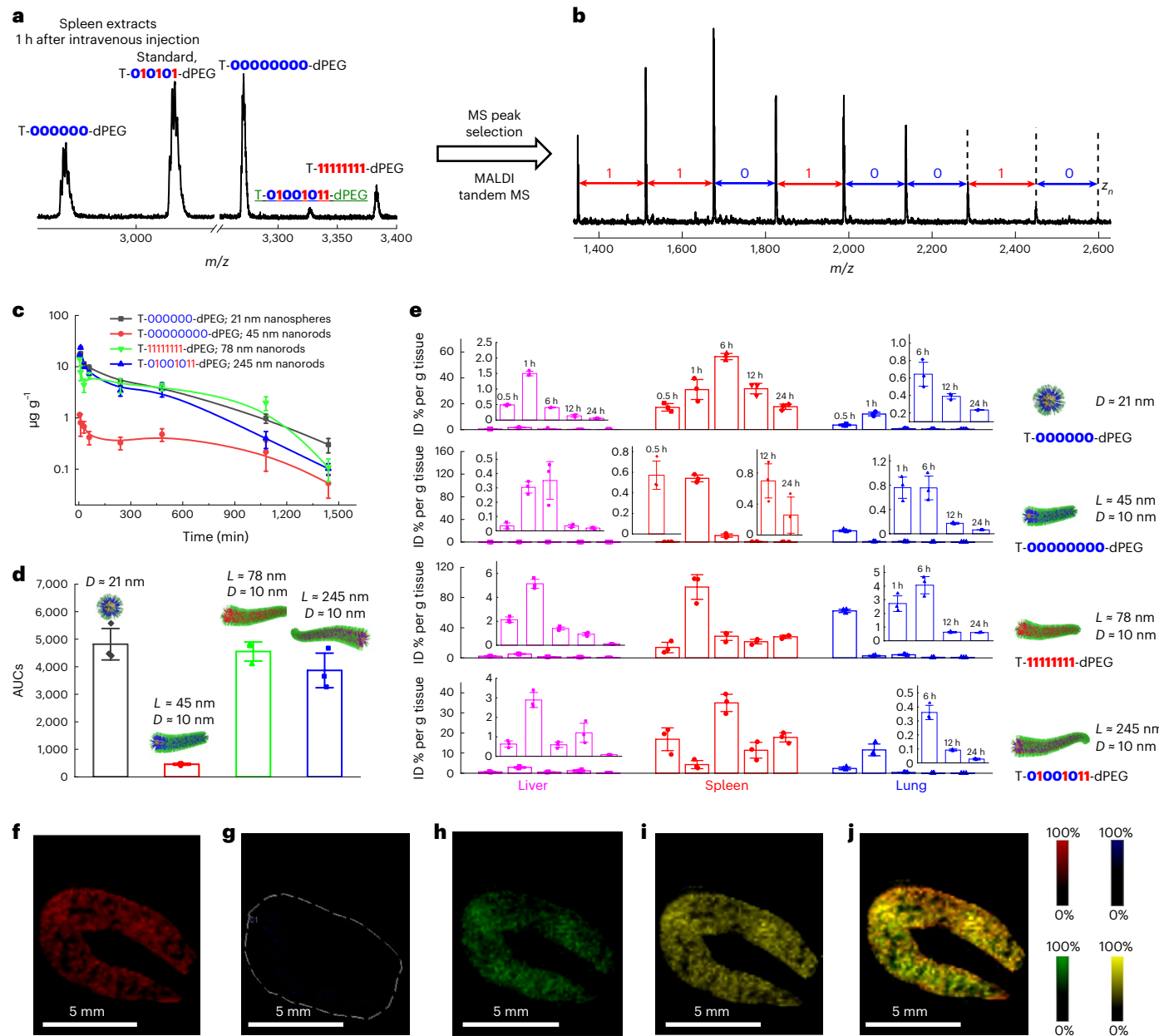


Fig. 6 | Identification and label-free quantification of digital micelles at organ and tissue slice levels. **a**, MALDI-TOF mass spectrum of spleen extracts from SD rats killed at 1 h after intravenous injection of a mixture of four types of digital micelles (21 nm nanospheres and 45 nm, 78 nm and 245 nm nanorods). **b**, Direct reading of the MS peak corresponding to T-01001011-dPEG shown in a with MALDI LIFT tandem MS. **c,d**, Pharmacokinetics ($n = 3$ biologically independent animals; data are presented as mean values \pm s.d.) (c) and areas under the pharmacokinetic curves (AUCs) quantified by MALDI-TOF MS (d) upon intravenous injection of a mixture of four types of digital micelles into SD rats ($n = 3$ biologically independent animals; data are presented as mean

values \pm s.e.m.). **e**, Label-free quantification of biodistributions in major organs by MALDI-TOF MS at 0.5, 1, 6, 12 and 24 h after intravenous injection of a mixture of four types of digital micelles into SD rats ($n = 3$ biologically independent animals; data are presented as mean values \pm s.e.m.). **f–j**, Typical MALDI images of 21 nm nanospheres (T-000000-dPEG) (f), 45 nm nanorods (T-0000000-dPEG) (g), 78 nm nanorods (T-1111111-dPEG) (h) and 245 nm nanorods (T-01001011-dPEG) (i), and corresponding overlay MALDI image (j) recorded for the spleen slice of rats killed at 0.5 h after intravenous injection of a mixture of four types of digital micelles.

the cells were washed with PBS buffer, trypsinized and freeze-dried, and extracted for further MALDI-TOF MS quantification. Over 0–12 h coinubcation, cellular uptake extents continually increase for all cell types. Among the four types of digital micelles, 78 nm nanorods exhibit the highest internalization (up to 17% at 12 h for HepG2 cells), compared with 0.27%, 1.5% and 1.25% for 21 nm nanospheres, 45 nm nanorods and 245 nm nanorods, respectively (Supplementary Fig. 79). The other three types of cells (4T1, LO2 and 3T3) consistently exhibit high cellular internalization towards 78 nm nanorods, with uptake extents at 12 h coinubcation

of 22.5%, 14.4% and 12.5%, respectively. Compared with nanorods with a diameter of ~10 nm and lengths in the range of 45–245 nm, 21 nm nanospheres exhibit the lowest cellular uptake (<0.5% at 12 h coinubcation for all cell types). Moreover, comparable internalization extents of cancer cells (HepG2 and 4T1) and normal cells (LO2 and 3T3) were observed for each type of digital micelle (Fig. 6c and Supplementary Figs. 79 and 80). These results imply that the conventional pegylation approach towards nanocarrier designs results in adverse effects^{4,5,7}, leading to weakening of NP–cell interactions and loss of cellular internalization selectivity².

However, the use of non-spherical NPs with optimized dimensions (for example, nanorods of median length as discussed above) and surface chemistries provides promising directions.

Chemical intuition suggests that encoded polymeric amphiphiles bear structural analogy to double-chain lipids conjugated with hydrophilic segments such as 1,2-distearoyl-*sn*-glycero-3-p-phosphoethanolamine-poly(ethylene glycol) (DSPE-PEG), except for the middle sequence-defined segment. Note that Food and Drug Administration-approved lipid nanoparticles for mRNA COVID-19 vaccines also contain PEG-based lipids with double-alkyl tails⁵⁸. To explore the design generality for digital micelles self-assembled from encoded amphiphiles, we further propose the concept of digital lipids by incorporating encoded oligourethane segments into conventional double-chain lipids. The design and synthesis of two prototype examples, 2C₁₈-**0000**-OEG₁₆-OH and 2C₁₈-**0101**-OEG₁₆-OH, are shown in Supplementary Schemes 24–26 and Supplementary Figs. 81–86. Next, delivery nanovehicles for small interfering RNA (FAM-siRNA-Luc) were constructed from cationic lipid-like G0-C14 (Supplementary Scheme 27 and Supplementary Fig. 87), poly(D,L-lactide-co-glycolide) (PLGA) and lecithin, which were stabilized by either DSPE-PEG or the digital lipid 2C₁₈-**0101**-OEG₁₆-OH for direct comparison⁵⁹ (Extended Data Fig. 4 and Supplementary Fig. 88). It was found that hybrid NPs assisted by 2C₁₈-**0101**-OEG₁₆-OH could efficiently encapsulate siRNA, exhibiting high stability and effectively transporting siRNA into live cells, behaviour comparable to that of NPs assisted by DSPE-PEG (Extended Data Fig. 5). Most importantly, the relative extents of internalized siRNA could be precisely quantified in a label-free manner by MALDI-TOF MS based on 2C₁₈-**0101**-OEG₁₆-OH, using 2C₁₈-**0000**-OEG₁₆-OH as an internal standard (Extended Data Fig. 5f and Supplementary Figs. 89 and 90). Note that this analysis is not possible for hybrid NPs assisted by DSPE-PEG, and conventional quantification through fluorescence of FAM-conjugated siRNA-Luc suffers from severe uncertainties⁷⁸. In addition, luciferase silencing assays revealed that internalized siRNA led to effective knockdown of the luciferase level (Extended Data Fig. 6).

These encoded polymeric amphiphiles could also serve as barcodes for the label-free quantification of micellar NPs self-assembled from amphiphilic BCps at cellular levels. To investigate this, three different BCps consisting of PEG and biodegradable poly(lactic acid) (PLA) blocks of varying lengths, mPEG_{2k}-PLA_n ($n = 20, 50, 100$), were first synthesized (Supplementary Scheme 28 and Supplementary Fig. 91). The subsequent microfluidic coassembly with three encoded amphiphiles of varying sequences, T-**0000000**-dPEG, T-**000000000**-dPEG and T-**01010101**-dPEG, respectively, fabricated three types of barcoded micellar NPs with various dimensions. Blank NPs without encoded amphiphiles as barcodes were also fabricated accordingly (Supplementary Figs. 92–94). Upon coincubating with 4T1 cells for 1, 4 and 12 h, the absolute internalized contents of barcoded micellar NPs were facilely quantified by MALDI-TOF MS in a label-free manner, revealing a dramatic size effect for the cellular uptake of pegylated polymeric NPs (Supplementary Figs. 95 and 96).

Label-free quantification and biodistributions of digital micelles at organ and tissue slice levels

Encouraged by the above results, we further evaluated the pharmacokinetics, biodistributions and transport/clearance processes of digital micelles by MALDI-TOF MS upon *in vivo* administration. As control, female SD rats were intravenously injected with PBS buffer and killed, dissected major organs and blood were homogenized and freeze-dried, and the residues were thoroughly extracted for further MALDI characterization. No background MS signals from relevant biological molecules could be discerned for blood, liver and spleen extracts in the molecular weight range corresponding to encoded polymeric amphiphiles (2.6–3.4 kDa; Supplementary Fig. 97), which is highly desirable for reliable and reproducible MALDI quantification.

Next, we examined the microstructural stability of digital micelles under *in vivo* conditions. Digital micelles coassembled from T-**000000000**-dPEG and T-**01010101**-dPEG (7/1, wt/wt; Supplementary Fig. 98) were first fabricated. Note that the coassembly was confirmed by both SAXS and cryo-TEM, which revealed the formation of nanorods of intermediate average length compared with those separately self-assembled from T-**000000000**-dPEG and T-**01010101**-dPEG (Fig. 5 and Supplementary Figs. 58–60). After intravenous administration of coassembled nanorods at a total dose of 2.5 mg kg⁻¹, the SD rats were killed at 2 h post-injection; their major organs were harvested and the extracts analysed by MALDI-TOF MS. It was found that the MS peak area ratios of T-**000000000**-dPEG relative to T-**01010101**-dPEG for spleen, lung, and liver extracts remained almost constant when compared with the original coassembled digital micelles, suggesting the robustness of the digital micelles (Supplementary Fig. 99). For subsequent pharmacokinetics and biodistribution assays, the aforementioned four types of digital micelles (1.0 mg ml⁻¹) were mixed in equal volumes, followed by intravenous injection. At predetermined intervals, SD rats were killed and the percentages of the injected dose for each type of digital micelle in blood and major organs were quantified by MALDI-TOF MS. Figure 6a shows a representative mass spectrum of spleen extracts at 0.5 h after intravenous injection, with MS peaks corresponding to the four types of digital micelles (note that T-**010101**-dPEG was added as an internal standard). Moreover, the sequence of corresponding precisely encoded polymeric amphiphiles could be directly read by MALDI tandem MS, facilitating further verification of different types of digital micelles (see T-**01010101**-dPEG as an example; Fig. 6b).

According to the pharmacokinetics shown in Fig. 6c, all digital micelles exhibit typical blood clearance profiles within 24 h, and the blood level of 45 nm nanorods (T-**000000000**-dPEG) remains dramatically low throughout the process upon intravenous injection. The areas under the pharmacokinetic curves (AUCs) of digital micelles are calculated to be 4,818.1, 459.4, 4,553.1 and 3,867.0 µg·min g⁻¹ for 21 nm nanospheres, 45 nm nanorods, 78 nm nanorods and 245 nm nanorods, respectively (Fig. 6d). These results confirm in a label-free manner the prominent effects of the physical characteristics of polymeric nanoparticles on *in vivo* circulation and elimination from blood compartments. Among the three types of nanorods, more elongated ones (78 and 245 nm) exhibit prolonged circulation in comparison with the 45 nm nanorods, which is consistent with a previous report¹². The biodistribution data collected from major organs reveal that spleen capture of all four types of digital micelle occurs in the early stages, and ~61% of injected 45 nm nanorods are retained within the spleen at 1 h post-injection (Fig. 6e and Supplementary Figs. 100–102), corresponding to the extremely low blood concentrations for 45 nm nanorods (Fig. 6c). At 12 and 24 h after intravenous injection, all digital micelles except 45 nm nanorods still accumulate and are retained in the spleen, whereas liver accumulation is not prominent on a weight-average basis (Fig. 6e). These results suggest that although liver accumulation could be attenuated to some extent, prominent capture of pegylated nanoparticles by the spleen, which is ~20 times lower in weight than the liver, needs to be seriously considered^{5,60}. Note that under conventional whole-body fluorescence imaging, the spleen tends to be neglected compared to the liver. For 78 nm nanorods of T-**000000000**-dPEG, prominent transfer from lung to spleen and liver occurs for the first 0.5–1 h after intravenous injection (Supplementary Fig. 100). On the other hand, MALDI MS signals of all four types of digital micelles could be detected in the kidney, with 245 nm nanorods exhibiting the highest extent (up to 1.8% at 1 h after intravenous injection; Supplementary Fig. 102). These results suggested that extended nanorods with a diameter of ~10 nm exhibit slightly higher renal excretion than shorter ones. In view of the comparative dimensions of 21 nm nanospheres and 28 nm nanorods with a ~10 nm diameter, the biodistributions of these two types of digital micelle in major organs were further quantified by MALDI-TOF MS using T-**010101**-dPEG as an internal standard,

revealing an intricate nanostructure size- and shape-dependent effect (Supplementary Figs. 95 and 103).

Due to the importance of spleen immune cells for the processing and clearance of exogenous organic NPs, the amounts of each digital micelle internalized by different types of immune cells and stromal cells within the spleen were further characterized. Major immune cells, including macrophages, T cells, B cells and dendritic cells, together with stromal cells, were sorted from the spleens of BALB/c mice killed at 1 or 6 h after intravenous injection of a mixture of four types of digital micelle (Extended Data Fig. 7, Supplementary Table 4, Supplementary Figs. 104–107, and Supplementary Table 5). The spleen extracellular matrix in the supernatant was also collected for further quantification. Due to the extremely low uptakes by specific types of spleen cells and the limitations of flow cytometry, we explored the use of heated electrospray ionization Fourier transform mass spectrometry (HESI-FTMS; Thermo Scientific Orbitrap Eclipse Tribrid module) for more reliable quantification. The established HESI-FTMS calibration curves indicated a detection limit down to $\sim 500 \text{ ng l}^{-1}$ or $\sim 0.17 \text{ nM}$ for these encoded amphiphiles (molecular weights in the range of $\sim 3.0 \text{ kDa}$; Supplementary Figs. 108 and 109), which is close to the maximum detection limit of the Orbitrap Eclipse apparatus ($\sim 100 \text{ ng l}^{-1}$ or 0.16 nM for reserpine; molecular weight, $\sim 0.6 \text{ kDa}$). These results indicated that the presence of a PEG dendron on encoded polymeric amphiphiles could also boost ESI-MS detection sensitivity via preferential ionization, following similar principles as observed for enhanced MALDI-TOFMS detection (Supplementary Fig. 56). Note that the HESI-FTMS detection limit of $\sim 0.17 \text{ nM}$ for encoded amphiphiles is ~ 600 -fold lower than that of conventional fluorescence techniques (typically up to $\sim 100 \text{ nM}$).

Among the four main types of immune cells, B cells and macrophages exhibit much higher average extents of cellular uptake of single cells at 6 h after intravenous injection of a mixture of the four types of digital micelles—although uptake varies depending on micellar size and shape—compared with those of T cells and dendritic cells (Extended Data Fig. 8), suggesting specific patterns of selective uptake by immune cells. At 1 h after intravenous injection, most of the digital micelles retained by the spleen are located within the extracellular matrix, and spleen B cells exhibit the lowest uptake of 245 nm nanorods (**T-01001011-dPEG**) compared with the other three types of digital micelles (Extended Data Fig. 8 and Supplementary Figs. 110 and 111). In addition, spleen stromal cells exhibit negligible internalization of all types of digital micelles at both 1 and 6 h after intravenous injection.

We then explored the possibility of MALDI identification and quantification on tissue slices sectioned from harvested organs of SD rats upon in vivo administration of a mixture of different types of digital micelles. Note that direct MALDI characterization of polymeric NPs within sliced tissues is complicated by interference from endogenous biomolecules and by the polydisperse nature of conventional synthetic polymers. Fortunately, MALDI-TOF MS spectra directly collected on sectioned tissues only reveal the set of peaks corresponding to the four types of digital micelles (Supplementary Fig. 112), further confirming the superiority of the MALDI technique over other labeling approaches^{28,29}. The facile identification of precisely encoded amphiphiles is ascribed to PEG-dendron-enhanced ionization and detection sensitivity, the elevated molecular weight range (bypassing interferences from lipids and small molecule metabolites) and the discrete molecular weights.

Next, we proceed to exploit MALDI imaging to directly monitor the spatial distribution of digital micelles on tissue slices. The obtained substructure distributions (Fig. 6f,j and Supplementary Figs. 113–115) are generally consistent with trends quantified from organ extracts (Fig. 6e). Specifically, MALDI signals of all four types of digital micelles in liver slices are below the detection limit, confirming the low extent of liver capture (Fig. 6e). MALDI imaging also reveals major retention of 78 nm nanorods in the lung at 0.5 h, and almost complete transfer from lung to spleen at 1 h after intravenous injection (Supplementary

Figs. 113 and 114). It is noteworthy that phagocytosis of pegylated digital micelles by the spleen, one of the major organs of the mono-nuclear phagocyte system, occurs as soon as 0.5 h after intravenous injection. Nanospheres (21 nm) and nanorods of 78 nm and 245 nm are mainly distributed in the splenic red pulp rather than in the white pulp. Compared to that at 0.5 h, spleen capture of 45 nm nanorods of **T-00000000-dPEG** is prominently enhanced at 1 h after intravenous injection. Most importantly, all four types of digital micelles exhibit non-uniform distributions within the spleen slice (Supplementary Fig. 115), implying distinct nanostructure shape effects on sub-organ spatiotemporal distributions. Using the liver tissue slice as a representative, the MALDI detection limits for digital micelles of **T-00000000-dPEG** and **T-01001011-dPEG** were determined to be ~ 5.9 and $\sim 3.7 \mu\text{g g}^{-1}$, respectively (Supplementary Figs. 116 and 117). Note that the detection limit of $\sim 1 \mu\text{M}$ at the tissue slice level is comparable to that of the fluorescence technique, although the latter suffers from limited detection channels and unavoidable background interference.

Finally, the microstructural stability and integrity of digital micelles under in vivo conditions was examined using the FRET technique on tissue slices from mice killed at specified time points. M_{D+A} nanospheres and M_{D+A} nanorods were coassembled from NBD-2C12-**000000-dPEG**, MS735-2C12-**000000-dPEG** and **T-000000-dPEG** (5/5/90, wt/wt/wt), and from BD-2C12-**000000-dPEG**, MS735-2C12-**000000-dPEG** and **T-01001011-dPEG** (5/5/90, wt/wt/wt), respectively (Supplementary Fig. 76). The FRET ratio for M_{D+A} nanorod dispersion was determined to be ~ 0.31 (Supplementary Fig. 118). At 6 h after intravenous injection of the M_{D+A} nanospheres and M_{D+A} nanorods into mice (Supplementary Fig. 119), the animals were killed and sectioned slices of major organs (that is, liver, spleen and lung) were characterized by confocal laser scanning microscopy to check the microstructural evolution of the digital micelles (Supplementary Figs. 120–123). High colocalization ratios between NBD and MS735 emission channels and negligible changes in FRET ratios verified that these digital micelles are stable even under in vivo conditions. These results are in agreement with the in vitro stability against FBS confirmed by both FRET and cryo-TEM data (Supplementary Figs. 64–68). In stark contrast, for liver, spleen and lung slices of BALB/c mice killed at 6 h after intravenous injection of a physical mixture of M_D nanorods and M_A nanospheres, no obvious FRET process could be discerned and the colocalization ratios between NBD and MS735 channels remained rather low (Supplementary Figs. 124 and 125), again verifying the microstructural stability of the digital micelles and the absence of any micellar exchange during the experimental time frame.

Conclusions

This work presents the first example of facile identification, direct reading and label-free quantification of digital micelles, which are self-assembled from synthetic polymers with built-in sequence information, from biological tissue samples. We envision that the PEG-dendron-boosted MALDI quantification and decoding strategy could be further utilized to sequence peptide/protein/DNA and other natural/synthetic molecular entities, and to probe relevant chemical/biological processes and transport pathways under both cellular and in vivo conditions. Moreover, digital micelles of precisely encoded amphiphiles and digital lipids capable of direct sequence reading and high-throughput MALDI quantification, as proposed in this work, represent new directions in fields ranging from surfactant and colloidal science to supramolecular chemistry, opening new avenues for understanding the in vivo fate of soft matter NPs and the design of next-generation nanomedicines.

Online content

Any methods, additional references, Nature Research reporting summaries, source data, extended data, supplementary information, acknowledgements, peer review information; details of

author contributions and competing interests; and statements of data and code availability are available at <https://doi.org/10.1038/s41557-022-01076-y>.

References

1. Anselmo, A. C. & Mitragotri, S. Nanoparticles in the clinic: an update. *Bioeng. Transl. Med.* **4**, e10143 (2019).
2. Shi, J. J., Kantoff, P. W., Wooster, R. & Farokhzad, O. C. Cancer nanomedicine: progress, challenges and opportunities. *Nat. Rev. Cancer* **17**, 20–37 (2017).
3. Wilhelm, S. et al. Analysis of nanoparticle delivery to tumours. *Nat. Rev. Mater.* **1**, 16014 (2016).
4. Sindhwan, S. et al. The entry of nanoparticles into solid tumours. *Nat. Mater.* **19**, 566–575 (2020).
5. Kunjachan, S., Ehling, J., Storm, G., Kiessling, F. & Lammers, T. Noninvasive imaging of nanomedicines and nanotheranostics: principles, progress, and prospects. *Chem. Rev.* **115**, 10907–10937 (2015).
6. Green, J. J. & Elisseeff, J. H. Mimicking biological functionality with polymers for biomedical applications. *Nature* **540**, 386–394 (2016).
7. Morsbach, S. et al. Engineering proteins at interfaces: from complementary characterization to material surfaces with designed functions. *Angew. Chem. Int. Ed.* **57**, 12626–12648 (2018).
8. Winzen, S., Koynov, K., Landfester, K. & Mohr, K. Fluorescence labels may significantly affect the protein adsorption on hydrophilic nanomaterials. *Colloid Surf. B* **147**, 124–128 (2016).
9. Kreyling, W. G. et al. In vivo integrity of polymer-coated gold nanoparticles. *Nat. Nanotechnol.* **10**, 619–623 (2015).
10. Meng, F. F., Wang, J. P., Ping, Q. N. & Yeo, Y. Quantitative assessment of nanoparticle biodistribution by fluorescence imaging, revisited. *ACS Nano* **12**, 6458–6468 (2018).
11. Zhao, Z. et al. Revisiting an ancient inorganic aggregation-induced emission system: an enlightenment to clusteroluminescence. *Aggregate* **2**, e36 (2021).
12. Geng, Y. et al. Shape effects of filaments versus spherical particles in flow and drug delivery. *Nat. Nanotechnol.* **2**, 249–255 (2007).
13. Lutz, J.-F., Lehn, J.-M., Meijer, E. W. & Matyjaszewski, K. From precision polymers to complex materials and systems. *Nat. Rev. Mater.* **1**, 16024 (2016).
14. Lutz, J.-F., Ouchi, M., Liu, D. R. & Sawamoto, M. Sequence-controlled polymers. *Science* **341**, 1238149 (2013).
15. Meier, M. A. R. & Barner-Kowollik, C. A new class of materials: sequence-defined macromolecules and their emerging applications. *Adv. Mater.* **31**, 1806027 (2019).
16. Lee, J. M. et al. Semiautomated synthesis of sequence-defined polymers for information storage. *Sci. Adv.* **8**, eabl8614 (2022).
17. Gunay, U. S. et al. Chemoselective synthesis of uniform sequence-coded polyurethanes and their use as molecular tags. *Chem.* **1**, 114–126 (2016).
18. Zydzik, N. et al. Coding and decoding libraries of sequence-defined functional copolymers synthesized via photoligation. *Nat. Commun.* **7**, 13672 (2016).
19. Martens, S. et al. Multifunctional sequence-defined macromolecules for chemical data storage. *Nat. Commun.* **9**, 4451 (2018).
20. Konig, N. F. et al. Photo-editable macromolecular information. *Nat. Commun.* **10**, 3774 (2019).
21. Song, B., Lu, D., Qin, A. & Tang, B. Z. Combining hydroxyl-yne and thiol-ene click reactions to facilely access sequence-defined macromolecules for high-density data storage. *J. Am. Chem. Soc.* **144**, 1672–1680 (2022).
22. Launay, K. et al. Precise alkoxyamine design to enable automated tandem mass spectrometry sequencing of digital poly(phosphodiester)s. *Angew. Chem. Int. Ed.* **60**, 917–926 (2020).
23. De Bruycker, K., Welle, A., Hirth, S., Blanksby, S. J. & Barner-Kowollik, C. Mass spectrometry as a tool to advance polymer science. *Nat. Rev. Chem.* **4**, 257–268 (2020).
24. Soete, M. & Du Prez, F. E. Sequencing of uniform multifunctional oligoesters via random chain cleavages. *Angew. Chem. Int. Ed.* **61**, e202202819 (2022).
25. Yan, X. Y. et al. Magnifying the structural components of biomembranes: a prototype for the study of the self-assembly of giant lipids. *Angew. Chem. Int. Ed.* **59**, 5226–5234 (2020).
26. Sternhagen, G. L. et al. Solution self-assemblies of sequence-defined ionic peptoid block copolymers. *J. Am. Chem. Soc.* **140**, 4100–4109 (2018).
27. Zhao, Z., He, W. & Tang, B. Z. Aggregate materials beyond alegens. *Acc. Mater. Res.* **2**, 1251–1260 (2021).
28. Yaari, Z. et al. Theranostic barcoded nanoparticles for personalized cancer medicine. *Nat. Commun.* **7**, 13325 (2016).
29. Dahlman, J. E. et al. Barcoded nanoparticles for high throughput in vivo discovery of targeted therapeutics. *Proc. Natl Acad. Sci. USA* **114**, 2060–2065 (2017).
30. Altuntas, E. & Schubert, U. S. ‘Polymeromics’: mass spectrometry based strategies in polymer science toward complete sequencing approaches: a review. *Anal. Chim. Acta* **808**, 56–69 (2014).
31. Liou, C. C. & Brodbelt, J. S. Determination of orders of relative alkali-metal ion affinities of crown ethers and acyclic analogs by the kinetic method. *J. Am. Soc. Mass. Spectrom.* **3**, 543–548 (1992).
32. Zhang, X. & Wang, C. Supramolecular amphiphiles. *Chem. Soc. Rev.* **40**, 94–101 (2011).
33. Huang, Z. et al. Binary tree-inspired digital dendrimer. *Nat. Commun.* **10**, 1918 (2019).
34. Holloway, J. O., Van Lijsebettens, F., Badi, N., Houck, H. A. & Du Prez, F. E. From sequence-defined macromolecules to macromolecular pin codes. *Adv. Sci.* **7**, 1903698 (2020).
35. Carl, P. L., Chakravarty, P. K. & Katzenellenbogen, J. A. A novel connector linkage applicable in prodrug design. *J. Med. Chem.* **24**, 479–480 (1981).
36. Sagi, A., Weinstein, R., Karton, N. & Shabat, D. Self-immolative polymers. *J. Am. Chem. Soc.* **130**, 5434–5435 (2008).
37. Shelef, O., Gnaim, S. & Shabat, D. Self-immolative polymers: an emerging class of degradable materials with distinct disassembly profiles. *J. Am. Chem. Soc.* **143**, 21177–21188 (2021).
38. Liu, G., Wang, X., Hu, J., Zhang, G. & Liu, S. Self-immolative polymersomes for high-efficiency triggered release and programmed enzymatic reactions. *J. Am. Chem. Soc.* **136**, 7492–7497 (2014).
39. Ding, Z. et al. Self-immolative nanoparticles for stimuli-triggered activation, covalent trapping and accumulation of in situ generated small molecule theranostic fragments. *Giant* **1**, 100012 (2020).
40. Cho, C. Y. et al. An unnatural biopolymer. *Science* **261**, 1303–1305 (1993).
41. Ghosh, A. K., Sarkar, A. & Brindisi, M. The Curtius rearrangement: mechanistic insight and recent applications in natural product syntheses. *Org. Biomol. Chem.* **16**, 2006–2027 (2018).
42. Takizawa, K., Tang, C. & Hawker, C. J. Molecularly defined caprolactone oligomers and polymers: synthesis and characterization. *J. Am. Chem. Soc.* **130**, 1718–1726 (2008).
43. Bott, G., Field, L. D. & Sternhell, S. Steric effects—a study of a rationally designed system. *J. Am. Chem. Soc.* **102**, 5618–5626 (1980).

44. Yoshimura, A., Luedtke, M. W. & Zhdankin, V. V. (Tosylimino) phenyl- λ^3 -iodane as a reagent for the synthesis of methyl carbamates via Hofmann rearrangement of aromatic and aliphatic carboxamides. *J. Org. Chem.* **77**, 2087–2091 (2012).
45. Mondal, T., Charles, L. & Lutz, J. F. Damage and repair in informational poly(*n*-substituted urethane)s. *Angew. Chem. Int. Ed.* **59**, 20390–20393 (2020).
46. Dahlhauser, S. D. et al. Sequencing of sequence-defined oligourethanes via controlled self-immolation. *J. Am. Chem. Soc.* **142**, 2744–2749 (2020).
47. Hu, X. L. et al. Polyprodrug amphiphiles: hierarchical assemblies for shape-regulated cellular internalization, trafficking, and drug delivery. *J. Am. Chem. Soc.* **135**, 17617–17629 (2013).
48. He, Y. et al. Uniform biodegradable fiber-like micelles and block coromicelles via ‘living’ crystallization-driven self-assembly of poly(L-lactide) block copolymers: the importance of reducing unimer self-nucleation via hydrogen bond disruption. *J. Am. Chem. Soc.* **141**, 19088–19098 (2019).
49. Li, L. et al. A general strategy toward synthesis of well-defined polypeptides with complex chain topologies. *CCS Chem.* **4**, <https://doi.org/10.31635/ccschem.31022.202101704> (2022).
50. Gilroy, J. B. et al. Monodisperse cylindrical micelles by crystallization-driven living self-assembly. *Nat. Chem.* **2**, 566–570 (2010).
51. Das, A. et al. Consequences of dispersity on the self-assembly of ABA-type amphiphilic block co-oligomers. *ACS Macro Lett.* **7**, 546–550 (2018).
52. Champion, J. A. & Mitragotri, S. Role of target geometry in phagocytosis. *Proc. Natl Acad. Sci. USA* **103**, 4930–4934 (2006).
53. Brown, T. D., Habibi, N., Wu, D., Lahann, J. & Mitragotri, S. Effect of nanoparticle composition, size, shape, and stiffness on penetration across the blood-brain barrier. *ACS Biomater. Eng.* **6**, 4916–4928 (2020).
54. Nguyen, H. V. T. et al. Bottlebrush polymers with flexible enantiomeric side chains display differential biological properties. *Nat. Chem.* **14**, 85–93 (2022).
55. Zhang, K. et al. Shape effects of nanoparticles conjugated with cell-penetrating peptide (HIV Tat PTD) on CHO cell uptake. *Bioconjugate Chem.* **19**, 1880–1887 (2008).
56. Gratton, S. E. A. et al. The effect of particle design on cellular internalization pathways. *Proc. Natl Acad. Sci. USA* **105**, 11613–11618 (2008).
57. Zhou, Q. et al. Enzyme-activatable polymer-drug conjugate augments tumour penetration and treatment efficacy. *Nat. Nanotechnol.* **14**, 799–809 (2019).
58. Hou, X., Zaks, T., Langer, R. & Dong, Y. Lipid nanoparticles for mRNA delivery. *Nat. Rev. Mater.* **6**, 1078–1094 (2021).
59. Zhu, X. et al. Long-circulating siRNA nanoparticles for validating prohibitin1-targeted non-small cell lung cancer treatment. *Proc. Natl Acad. Sci. USA* **112**, 7779–7784 (2015).
60. Bourquin, J. et al. Biodistribution, clearance, and long-term fate of clinically relevant nanomaterials. *Adv. Mater.* **30**, 1704307 (2018).

Publisher's note Springer Nature remains neutral with regard to jurisdictional claims in published maps and institutional affiliations.

Springer Nature or its licensor (e.g. a society or other partner) holds exclusive rights to this article under a publishing agreement with the author(s) or other rightsholder(s); author self-archiving of the accepted manuscript version of this article is solely governed by the terms of such publishing agreement and applicable law.

© The Author(s), under exclusive licence to Springer Nature Limited 2022

Methods

Materials

Triethylene glycol monomethyl ether, DCTB and sodium trifluoroacetate were purchased from Sigma-Aldrich and used as received. Phytol, Raney nickel catalyst, 3,4-dihydroxybenzaldehyde, *tert*-butyldimethylsilyl chloride (TBSCl), diphenylphosphoryl azide (DPPA), 4-(hydroxymethyl)benzoic acid, 4-bromo-3-methylbenzoic acid, 4-(hydroxymethyl)benzonitrile, tetrabutylammonium hydrogen sulfate, 4-cyano-3-methylbenzoic acid, 2-nitro-4,5-dimethoxybenzyl alcohol (NVOC), terephthalaldehyde, imidazole, sodium chlorite (NaClO_2), 2-methyl-2-butene, 3,5-dihydroxybenzoic acid, 3-chloro-2-chloromethyl-1-propene, 3-formylbenzoic acid, 60% NaH (dispersion in mineral oil), borane–tetrahydrofuran complex (1.0 M), trifluoroacetic acid (TFA), anhydrous triethylamine (TEA), anhydrous *N,N*-dimethylformamide (DMF), anhydrous 2-methyltetrahydrofuran (MeTHF), *n*-butyllithium (1.6 M), 30% hydrogen peroxide aqueous solution (30% H_2O_2) and all other chemicals/reagents were purchased from commercial sources and used as received. FBS, penicillin, streptomycin and Dulbecco's modified Eagle's medium (DMEM) were purchased from GIBCO and used as received. Anhydrous THF, MeCN, DCM and toluene were collected from the Innovative Technology PS-MD-5 solvent purification system. (S)-(2,2-Dimethyl-1,3-dioxolane-4-methanol, sodium hydride (NaH), 4-dimethylaminopyridine (DMAP), tetrabutylammonium iodide (TBAI), stearic acid, palladium on carbon (Pd/C), poly(amidoamine) (PAMAM) dendrimer (ethylenediamine core, generation 0.0), 1,2-epoxytetradecane, 12-aminododecan-1-ol, 9-fluorenylmethyl chloroformate (Fmoc-Cl), methyl 3,5-dihydroxybenzoate, 1-bromododecane, triphenylphosphine (PPh_3), diisopropyl azodicarboxylate (DIAD), (E)-1-(5-carboxypentyl)-4-(2-(6-(diethylamino)benzofuran-2-yl)vinyl)pyridin-1-ium-3-sulfonate (MS735-COOH), 7-nitrobenzoxadiazole-6-amino hexanoic acid (NBD-COOH), benzotriazolyloxy-tris[pyrrolidino]-phosphonium hexafluorophosphate (PyBOP), tris(2-dimethylaminoethyl)amine (Me_6TREN), DL-lactide (DL-LA), 1-(3,5-bis-(trifluoromethyl)phenyl)-3-cyclohexylthiourea (TU), poly(ethylene oxide) monomethyl ether (mPEG_{2k}-OH, $M_n = 2.0$ kDa, $M_w/M_n = 1.06$), ester-terminated PLGA, 1,1'-di-*n*-octadecyl-3,3,3',3'-tetradethylinocarbocyanine perchlorate (DiI), 1,1'-dioctadecyl-3,3,3',3'-tetramethylindodicarbocyanine perchlorate (DiO), Nile red and lecithin were purchased from commercial sources and used as received. DSPE-PEG (PEG segment, 2.0 kDa) was obtained from Avanti Polar Lipids. FAM-conjugated siRNA targeting luciferase (FAM-siRNA-Luc) was purchased from Inovogen. Anti-CD45-APC, anti-CD3-PerCP Cy5.5, anti-CD45-APC, anti-B220/CD45R-BV510, anti-CD11c-FITC, anti-CD80-PE, anti-CD11b-BV650 and anti-F4/80-PE were purchased from BD Horizon. Water was deionized with a Milli-Q SP reagent water system (Millipore) to a specific resistivity of 18.4 MΩ·cm. 4-(Hydroxymethyl)benzaldehyde⁶¹ and PhINTs¹⁴ were synthesized according to literature procedures.

Modular synthesis of sequence-defined polymeric amphiphiles

Synthetic routes employed for the preparation of all monomeric and dimeric building blocks, light-sensitive trigger (T), hydrophilic dendron (dPEG), sequence-defined polyurethanes and corresponding encoded polymeric amphiphiles are shown in Fig. 2b and Supplementary Schemes 1–21. Detailed procedures and characterization data are described in Supplementary Figs. 1–39. Typical procedures for the synthesis of T-00000000-dPEG from T-0000000-OH and dPEG-AA are described below. dPEG-AA (3.0 equiv.) was dissolved in anhydrous toluene in a flame-dried reaction flask. After azeotropically removing all the solvents under reduced pressure, another portion of anhydrous toluene was added and the azeotropic distillation cycle was repeated three times. Next, anhydrous MeTHF was added and the mixture was stirred at 80 °C for 4 h under an argon atmosphere. The reaction progress was monitored by TLC. Upon completion, the

reaction mixture was cooled down to room temperature, and all the solvents were removed under reduced pressure at room temperature; the obtained dPEG-NCO was directly used for the next step without further purification. Into another reaction flask, T-00000000-OH (1.0 equiv.), catalytic equivalent DBTL and anhydrous toluene were charged. After three cycles of azeotropic distillation, MeTHF was added under the protection of an argon atmosphere. The solution was transferred into the previous reaction flask containing dPEG-NCO through a double-tipped stainless steel needle. The reaction mixture was stirred for 24 h at room temperature under an argon atmosphere protection. Subsequent precipitation into an excess of methanol and further purification by recycling preparative GPC (THF as eluent) afforded sequence-defined amphiphilic octameric polyurethane, T-00000000-dPEG. ¹H NMR (CDCl_3 ; DMSO-*d*₆ = 1:1 (v:v), δ , ppm, TMS; Supplementary Fig. 15f): δ 9.88–9.33 (m, 10H), 8.14 (s, 4H), 7.75–7.18 (m, 31H), 6.82 (s, 2H), 5.53 (d, $J = 48.7$ Hz, 4H), 5.06 (s, 14H), 4.21–3.82 (m, 12H), 3.49 (dt, $J = 47.7, 9.5$ Hz, 136H), 2.36–2.20 (m, 3H), 0.82 (s, 84H). MALDI-TOF MS (Fig. 2c,f): *m/z* calcd for [M + Na]⁺, 3,268.77; exp., 3,269.53.

Self-assembly of encoded polymeric amphiphiles into digital micelles

Typical procedures for the self-assembly of encoded amphiphiles are as follows. Into a capped vial (15 ml) equipped with a magnetic stirring bar, T-00000000-dPEG (1.0 mg) and 1,4-dioxane (1.0 ml) were added. The vial was maintained at 25 °C and stirred for 2 h. Deionized water (9 ml) was added through a syringe pump at a rate of 1.0 ml h⁻¹ at 25 °C under magnetic stirring (500 r.p.m.). Upon completion, the aqueous dispersion was stirred for an additional 2 h and dialysed against deionized water (molecular weight cut-off (MWCO), ~30 kDa) for 12 h, and fresh deionized water was replaced approximately every 2 h.

Fabrication of mixed micelles through coassembly of T-00000000-dPEG and T-01001011-dPEG

T-00000000-dPEG and T-01001011-dPEG (1.0 mg in total; 7:1 wt/wt) were dissolved in 1 ml 1,4-dioxane under magnetic stirring at 25 °C for 2 h. Deionized water (9 ml) was added through a syringe pump at a rate of 1.0 ml h⁻¹ at 25 °C under magnetic stirring (500 r.p.m.). Upon completion, the aqueous dispersion was stirred for an additional 2 h and dialysed against deionized water (MWCO, ~30 kDa) for 12 h, and fresh deionized water was replaced approximately every 2 h.

Cryo-TEM sample preparation

An aqueous dispersion (6 µl) containing nanostructures self-assembled from encoded polymeric amphiphiles (0.1 mg ml⁻¹) was dropped onto a lacey carbon-film-supported TEM copper grid (Cu-200LC, Pacific Grid-Tech). All TEM grids used for cryo-TEM imaging were pretreated with plasma air to render the lacey carbon film hydrophilic. A thin film of the sample solution was produced using a Vitrobot with a controlled humidity chamber (FEI). After loading the sample solution, the lacey carbon grid was blotted using preset parameters and plunged instantly into a liquid ethane reservoir precooled by liquid nitrogen. The vitrified samples were then transferred to a cryo-holder and cryo-transfer stage that was cooled by liquid nitrogen. To prevent sublimation of vitreous water, the cryo-holder temperature was maintained below –170 °C during the imaging process. Cryo-TEM analyses were conducted on a FEI Talos F200C microscope operating at 200 kV.

Processing of cryo-TEM data

For nanorods and nanofibres, Mezzenga et al.⁶² have developed an open-source software, FiberApp, to track and analyse these elongated nanostructures. FiberApp can easily handle TEM, atomic force microscopy and confocal microscopy images. The diameters and lengths of single nanorods were tracked using this software and ~200 nanorods were counted for each type of digital nanoassembly. L_n and L_w were quantitatively deduced from these data based on the following

equations (L = nanorod length, N = number)⁵⁰.

$$L_n = \frac{\sum_{i=1}^n N_i L_i}{\sum_{i=1}^n N_i} \quad (1)$$

$$L_w = \frac{\sum_{i=1}^n N_i L_i^2}{\sum_{i=1}^n N_i L_i} \quad (2)$$

$$\frac{L_w}{L_n} - 1 = \left(\frac{\sigma}{L_n} \right)^2 \quad (3)$$

The standard deviation (σ) of measured nanorod lengths is correlated with the length polydispersity (L_w/L_n).

MALDI-TOF MS characterization and sample preparation

MALDI-TOF mass spectra were acquired on an Autoflex Speed MALDI-TOF mass spectrometer (Bruker Daltonics) equipped with a Smart beam-II laser (355 nm, 1 kHz, Bruker Daltonics). The reflectron positive-ion mode was used for measurements with m/z ranges of 500–2,000 and 1,000–4,000 Da. The MALDI-TOF tandem mass spectra for specified precursors were recorded by using the Bruker LIFT module. The instrument was calibrated prior to each measurement with an external PMMA standard and peptide calibration standard II (Bruker Daltonics) around the investigated molecular weight range. All MALDI-TOF mass spectra were processed with the Compass for flexSeries 1.4 software package (Bruker Daltonics).

The ‘sandwich’ technique was used for MALDI sample preparation, and typical protocols are described below. DCTB matrix was dissolved in CH_3Cl_2 at a concentration of 20 mg ml⁻¹, and the cationizing agent, sodium trifluoroacetate, was dissolved in methanol at a concentration of 10 mg ml⁻¹. Freshly prepared DCTB and sodium trifluoroacetate solutions were mixed at a ratio of 10/1 (v/v). First, 2 μl of DCTB/sodium trifluoroacetate solution mixture was applied onto the MALDI stainless steel target plate; after brief drying (~30 s) under an air flow inside a laminar flow bench, THF solution (2 μl , ~5.0 g l⁻¹) of either encoded polymeric amphiphiles, synthetic intermediates or extracts from cells and rat organs was applied. After brief drying under an air flow (~30 s), another 2 μl of DCTB/sodium trifluoroacetate solution mixture was applied. After further drying for ~2 h under an air flow inside the laminar flow bench, the target plate was ready to be inserted into the MALDI-TOF mass spectrometer for analysis. The extent of laser attenuation was adjusted to minimize undesired polymer fragmentation and to maximize detection sensitivity.

Establishment of standard calibration curves for MALDI-TOF MS quantification

T-010101-dPEG was used as the internal standard for MALDI-TOF MS quantification of T-000000-dPEG, T-00000000-dPEG, T-01001011-dPEG and T-11111111-dPEG. During sample preparation for MALDI-TOF MS quantification, the solution concentration of internal standard (T-010101-dPEG) in THF was maintained constant (1.0 mg ml⁻¹). Typical procedures for construction of the T-000000-dPEG calibration curve are described below. T-000000-dPEG stock solution in THF (2.0 mg ml⁻¹) was prepared first. Next, 50, 100, 150, 200 and 250 μl stock solution were added into a series of 2 ml glass vials. After removing all the solvents under nitrogen purging, 200 μl solution of the internal standard, T-010101-dPEG, in THF was added to each vial. Thus, the concentrations of T-000000-dPEG are in the range of 0.5–2.5 mg ml⁻¹. The above solution was then subjected to primary MALDI-TOF MS characterization. The ratios of the primary MS peak areas of T-000000-dPEG relative to that of T-010101-dPEG were plotted against T-000000-dPEG concentrations to construct the standard calibration curve. Following

similar procedures described above, standard calibration curves of T-00000000-dPEG, T-01001011-dPEG and T-11111111-dPEG were also established (Fig. 6b).

Unexpected direct reading of sequence-defined amphiphilic polyurethanes via MALDI tandem MS

A series of sequence-defined polymeric amphiphiles containing oligourethane segments were analysed using MALDI tandem mass spectrometry (Bruker LIFT module) to decode oligourethane sequences. A 2 μl portion of a solution of sequence-defined polymeric amphiphiles in THF was utilized for MALDI-TOF MS sample preparation. The primary MALDI-TOF mass spectra were measured first, and MALDI tandem mass spectra for selected precursor ions were then determined using the Bruker LIFT module.

Cell culture and in vitro uptake of digital micelles assayed by MALDI-TOF MS

3T3 (mouse fibroblast cells, catalogue number 3101MOGNM6), 4T1 (mouse breast cancer cells, catalogue number 3101MOUSCSP5056) and HepG2 (human hepatocellular carcinoma cells, catalogue number 3101HUMSCSP510) obtained from the cell bank of the Chinese Academy of Science, and LO2 (human normal liver cell, catalogue number ZQ0031) obtained from Cell Research, were incubated in DMEM supplemented with 10% FBS and 1% antibiotics (penicillin–streptomycin) at 37 °C in a CO₂/air (5/95) incubator. 3T3, 4T1, LO2 and HepG2 cells were seeded into a six-well plate at a density of 4×10^5 cells per well and cultured at 37 °C for 24 h. Next, an aqueous dispersion containing a mixture of four types of digital micelles of T-000000-dPEG (21 nm spherical micelles), T-00000000-dPEG (45 nm nanorods), T-11111111-dPEG (78 nm nanorods) and T-01001011-dPEG (245 nm nanorods) was added to reach a total concentration of 0.4 mg ml⁻¹ in each well (0.1 mg ml⁻¹ for each type of digital micelle), followed by the addition of the calculated volume of concentrated DMEM to compensate for fluctuations in culture medium composition and ionic strength. After incubating for a specified time, the cell culture medium was removed and cells were washed three times with PBS buffer. The cells were suspended by treating with trypsin at 37 °C for 1 min, followed by the addition of DMEM supplemented with 10% FBS. The cell dispersion was centrifuged at 1,000 r.p.m. for 3 min. The supernatant solution was removed and cells were resuspended in 500 μl PBS buffer. After freeze-drying, the residues were mixed with 5 ml THF and stirred overnight at room temperature. After centrifugation at 5,000 r.p.m. for 5 min, the supernatant solution was collected and evaporated to dryness under reduced pressure. The residues were dissolved in THF and subjected to further MALDI-TOF MS analysis for quantification based on established standard calibration curves using T-010101-dPEG as the internal standard.

Pharmacokinetic studies upon intravenous injection of a mixture of four types of digital micelles

All animal experiments involved in this work were performed following a protocol approved by the Institutional Animal Care and Use Committee (University of Science and Technology of China). Healthy female SD rats (200–300 g, 10 weeks old) were purchased from Experimental Animal Center of Anhui Medical University. All animals were maintained on a 12 h/12 h light/dark cycle at 23–25 °C and 48–52% humidity. Aqueous dispersions of four types of digital micelles (1.0 mg ml⁻¹) of T-000000-dPEG (21 nm spherical micelles), T-00000000-dPEG (45 nm nanorods), T-11111111-dPEG (78 nm nanorods) and T-01001011-dPEG (245 nm nanorods) were mixed in equal volumes. For pharmacokinetic studies, the aqueous dispersion containing a mixture of the four types of digital micelles was injected via the tail vein into SD rats at a dosage of 2.5 mg kg⁻¹. At predetermined time points (5, 10, 30, 60, 240, 480, 1,080 and 1,440 min), tail vein bleeds (~200 μl) were collected into heparinized tubes and weighed.

Upon completion of the experiment, the rats were killed and all collected plasma samples were lyophilized. THF (2.0 ml) was added into each tube and the mixture was stirred at room temperature for 12 h, and then passed through a 450 nm PTFE membrane filter. Additional washing of the sampling tube with THF and filtration through the same membrane filter were repeated three times. The combined filtrates were evaporated to dryness under reduced pressure. The residues were dissolved in THF and subjected to further MALDI-TOF MS analysis for quantification based on established standard calibration curves.

Biodistributions in major organs upon intravenous injection of a mixture of four types of digital micelles

Aqueous dispersions of four types of digital micelles (1.0 mg ml⁻¹) of **T-000000-dPEG** (21 nm spherical micelles), **T-00000000-dPEG** (45 nm nanorods), **T-1111111-dPEG** (78 nm nanorods) and **T-01001011-dPEG** (245 nm nanorods) were mixed in equal volumes. An aqueous dispersion containing a mixture of the four types of digital micelles was injected via a tail vein into SD rats at a dosage of 2.5 mg kg⁻¹. At 0.5, 1, 6, 12 and 24 h after intravenous injection, rats were killed. Major organs were harvested, weighed and homogenized on a tissue grinder. After freeze-drying, the residues corresponding to each major organ were mixed with 20 ml THF and stirred overnight at room temperature. After passing through a 220 nm filter membrane, additional steps of extraction, washing with THF and filtration were repeated three times. All filtrates were combined and then evaporated to dryness under reduced pressure. The residues were dispersed in THF and subjected to further MALDI-TOF MS analysis for quantification based on established standard calibration curves.

Tissue sectioning and matrix application for MALDI imaging sample preparation

Sections from frozen tissues were collected on a cryostat at 10 µm thickness and thaw mounted onto indium-tin-oxide-coated conductive glass slides (Bruker Daltonics). The matrix solution consists of DCTB (15 mg ml⁻¹) and sodium trifluoroacetate (1 mg ml⁻¹) in CH₂Cl₂/methanol (1/2, v/v). The sections were coated on an ImagePrep instrument (Bruker Daltonics) with the following parameters: 25 cycles; spray power, 15%; modulation, 15%; spray time, 20 s; incubation time, 10 s; dry time, 10 s.

MALDI MS imaging acquisition

All MALDI-TOF MS imaging experiments were performed on an Autoflex Speed III MALDI-TOF mass spectrometer (Bruker Daltonics) in reflectron positive-ion mode. Mass spectra data sets were acquired over the whole tissue section over the *m/z* range of 2,800–3,400 Da. The laser beam size was set to 'large' and the laser energy was optimized for signal-to-noise ratios in each experiment. For image acquisition, a 50 µm raster width was selected and 500 individual mass spectra were acquired at 2 kHz repetition rate and accumulated for each pixel. Selection of measurement regions and visualization of images were performed with FlexImaging 4.1 software (Bruker Daltonics).

Theoretical calculation of BDEs

Geometry optimizations and frequency calculations were performed at the B3LYP-D3(BJ)/6-31G** level^{63,64}, with D3 denoting Grimme's dispersion interaction correction method. Single-point energies were calculated at the B3LYP-D3(BJ)/6-311 + G(2d,p) level^{65,66}. The BDE was obtained as the difference between the energy of fragments and entire molecules. All calculations were performed using the Gaussian 09 package.

Statistics and reproducibility

All experiments were conducted three times for each sample, and the results are consistent and repeatable in Fig. 5a–f, Extended Data Fig. 4b,

Extended Data Fig. 5g, and Supplementary Figs. 57a–d, 59a–d, 60a–d, 61a,b, 66–68, 78c, 88a, 94a–f, 98b, 120, 122 and 124.

Reporting summary

Further information on research design is available in the Nature Research Reporting Summary linked to this article.

Data availability

The authors declare that all data supporting the findings of this study are available within the article, the associated source data and its Supporting Information and can also be obtained from the corresponding author upon reasonable request. Source data are provided with this paper.

References

61. Zhang, H., Xie, F., Cheng, M. & Peng, F. Novel meta-iodobenzylguanidine-based copper thiosemicarbazide-1-guanidinomethylbenzyl anticancer compounds targeting norepinephrine transporter in neuroblastoma. *J. Med. Chem.* **62**, 6985–6991 (2019).
62. Usov, I. & Mezzenga, R. Fiberapp: an open-source software for tracking and analyzing polymers, filaments, biomacromolecules, and fibrous objects. *Macromolecules* **48**, 1269–1280 (2015).
63. Franci, M. M. et al. Self-consistent molecular orbital methods. XXIII. A polarization-type basis set for second-row elements. *J. Chem. Phys.* **77**, 3654–3665 (1982).
64. Grimme, S., Ehrlich, S. & Goerigk, L. Effect of the damping function in dispersion corrected density functional theory. *J. Comput. Chem.* **32**, 1456–1465 (2011).
65. Krishnan, R., Binkley, J. S., Seeger, R. & Pople, J. A. Self-consistent molecular orbital methods. XX. A basis set for correlated wave functions. *J. Chem. Phys.* **72**, 650–654 (1980).
66. Marenich, A. V., Cramer, C. J. & Truhlar, D. G. Universal solvation model based on solute electron density and on a continuum model of the solvent defined by the bulk dielectric constant and atomic surface tensions. *J. Phys. Chem. B* **113**, 6378–6396 (2009).

Acknowledgements

Financial support from the National Key Research and Development Program of China (2020YFA0710700), the National Natural Science Foundation of China (NNSFC) Project (51690150, 51690154, 52021002, 21925107 and U19A2094) and Fundamental Research Funds for the Central Universities is gratefully acknowledged. This work was partially carried out at the USTC Center for Micro and Nanoscale Research and Fabrication. We thank the staff from the BL19U2 beamline of the National Facility for Protein Science in Shanghai (NFPS) at the Shanghai Synchrotron Radiation Facility for assistance during SAXS data collection.

Author contributions

S.Y.L. conceived and thoroughly supervised the project. S.Y.L. and Q.Q.S. designed the experiments and analysed the data. Q.Q.S. conducted the experiments with assistance from R.D.S., J.X., J.J.T., X.Z. and J.C. MALDI-TOF MS and MALDI imaging experiments were conducted with help from H.Y. and Z.B.Z. Cryo-TEM characterization was conducted with help from H.M.T., C.H.C. and Y.F.Z. ESI-MS characterization and MS data interpretation were conducted with assistance from X.P.L. Q.Q.S., Z.Y.D., X.P.L. and S.Y.L. wrote the manuscript.

Competing interests

The authors declare no competing interests.

Additional information

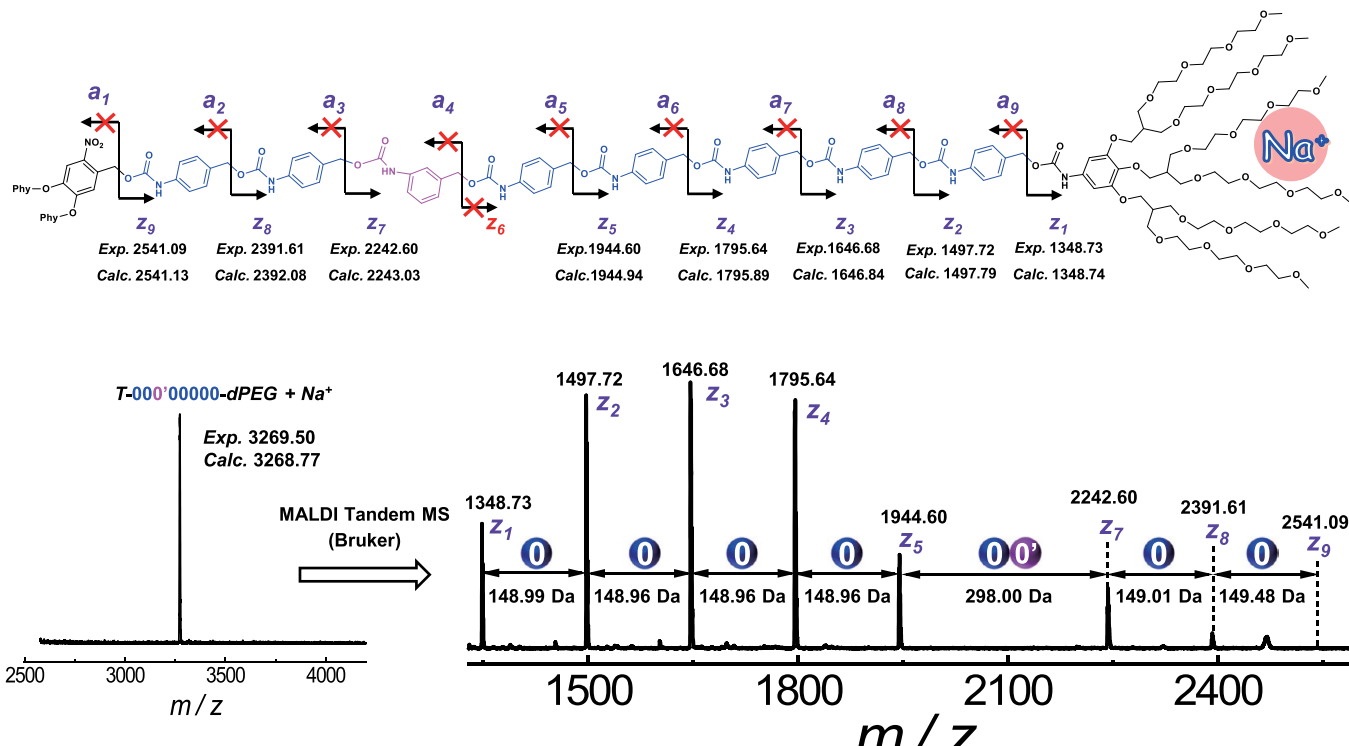
Extended data is available for this paper at <https://doi.org/10.1038/s41557-022-01076-y>.

Supplementary information The online version contains supplementary material available at <https://doi.org/10.1038/s41557-022-01076-y>.

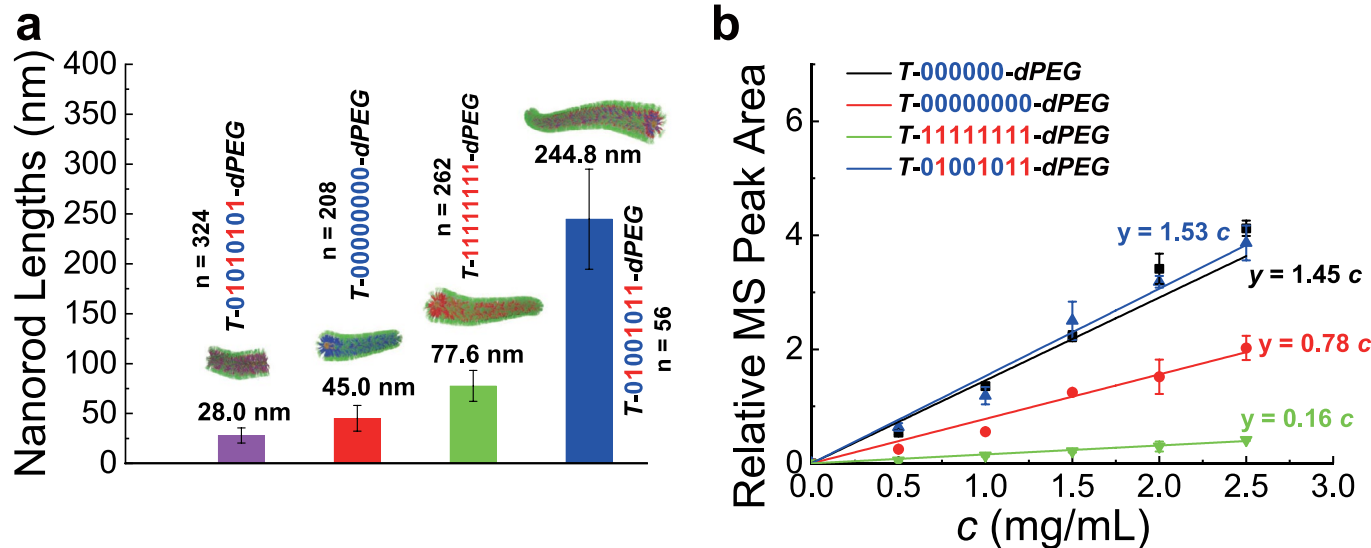
Correspondence and requests for materials should be addressed to Shiyong Liu.

Peer review information *Nature Chemistry* thanks Kanjiro Miyata, Donghui Zhang and the other, anonymous, reviewer(s) for their contribution to the peer review of this work.

Reprints and permissions information is available at www.nature.com/reprints.

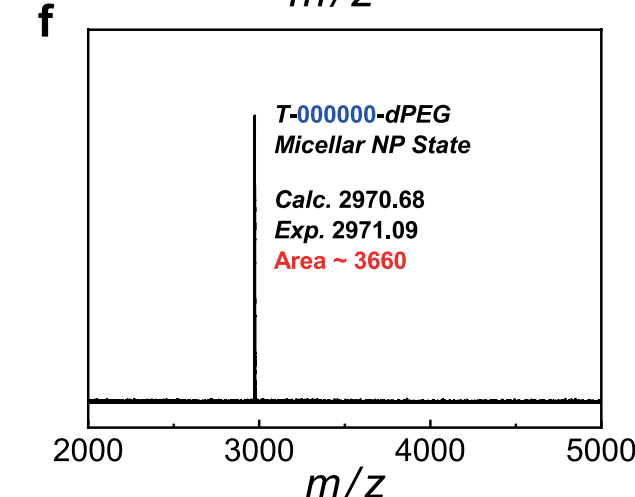
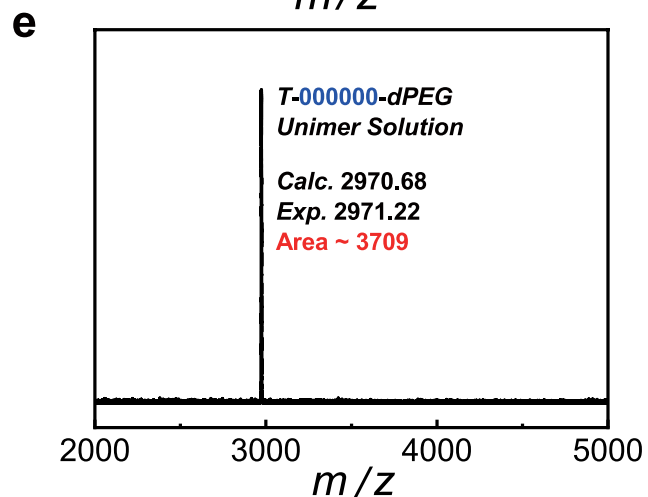
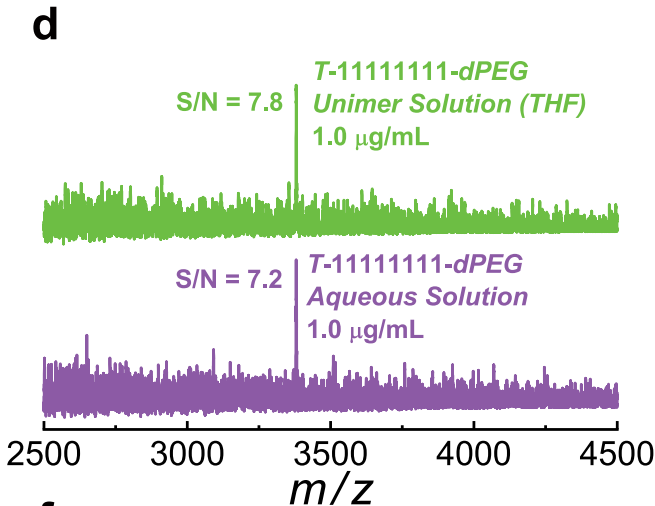
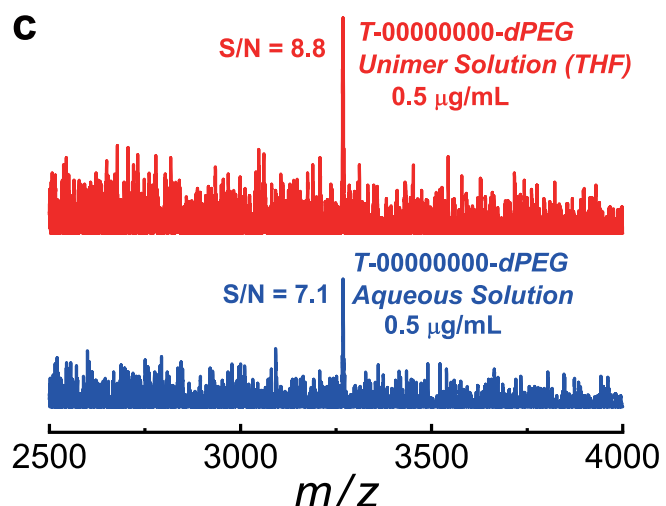
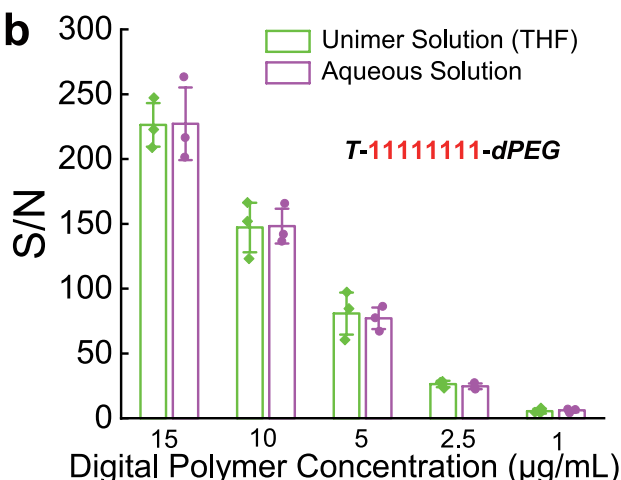
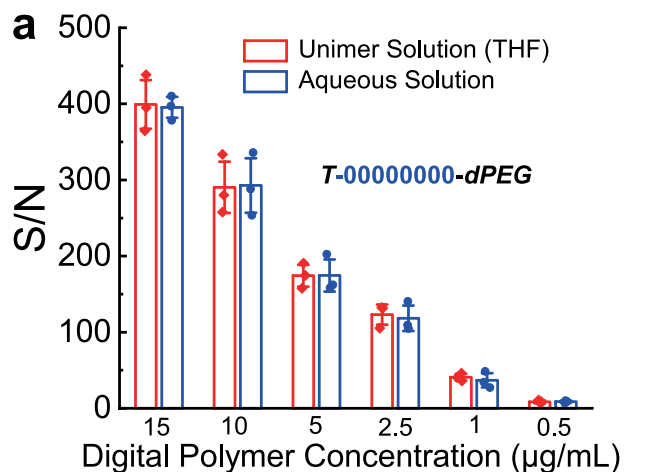


Extended Data Fig. 1 | Sequence reading of encoded amphiphiles. MALDI tandem MS recorded for T-000'00000-dPEG + Na^+ ; the benzyl-O linkage in O' unit (pink) remains inert and does not undergo fragmentation, indicating the bond-selective nature.



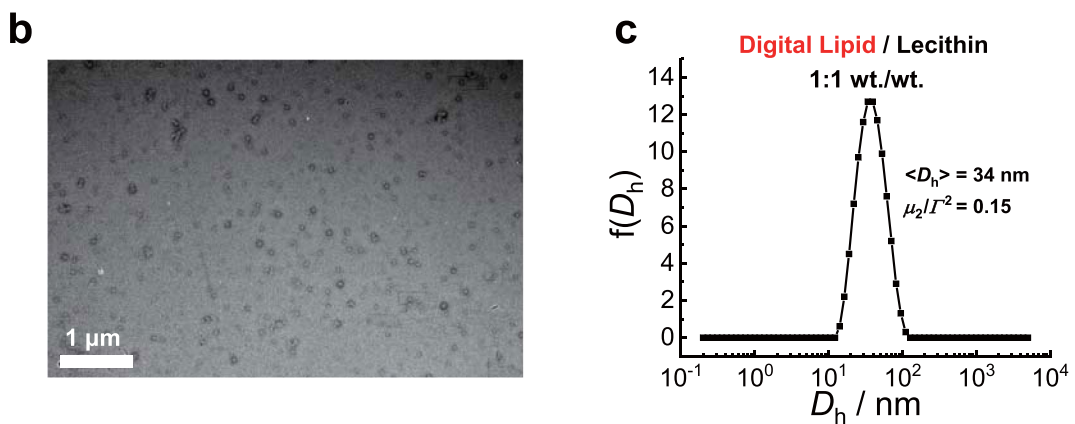
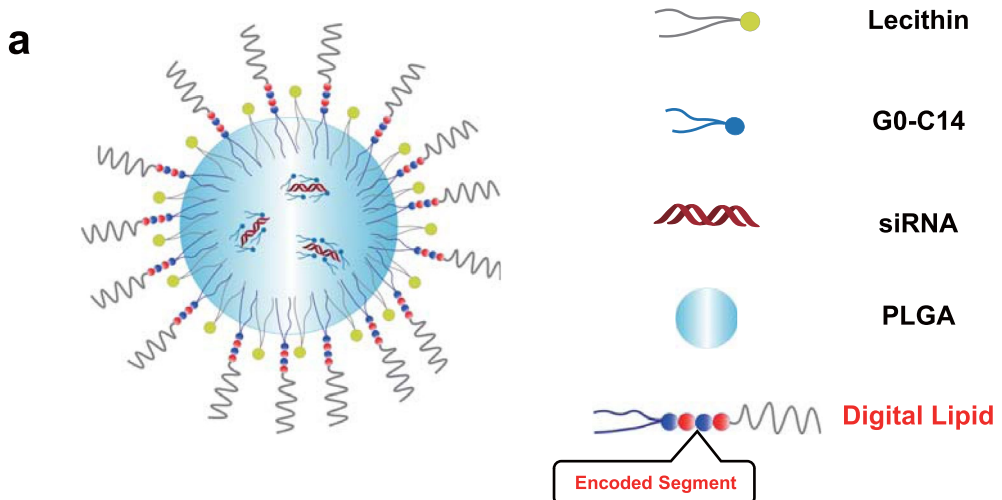
Extended Data Fig. 2 | Characterization of self-assembled nanorods and quantification of encoded amphiphiles. **a**, Sequence-regulated evolution of self-assembled nanorod lengths (n represents the number of digital micelles measured, data are presented as mean values \pm SD). **b**, Standard calibration

curves of sequence-defined polyurethanes relative to the control (T-010101-dPEG) for MALDI-TOF MS quantification (n = 3 independent experiments; data are presented as mean values \pm SD).

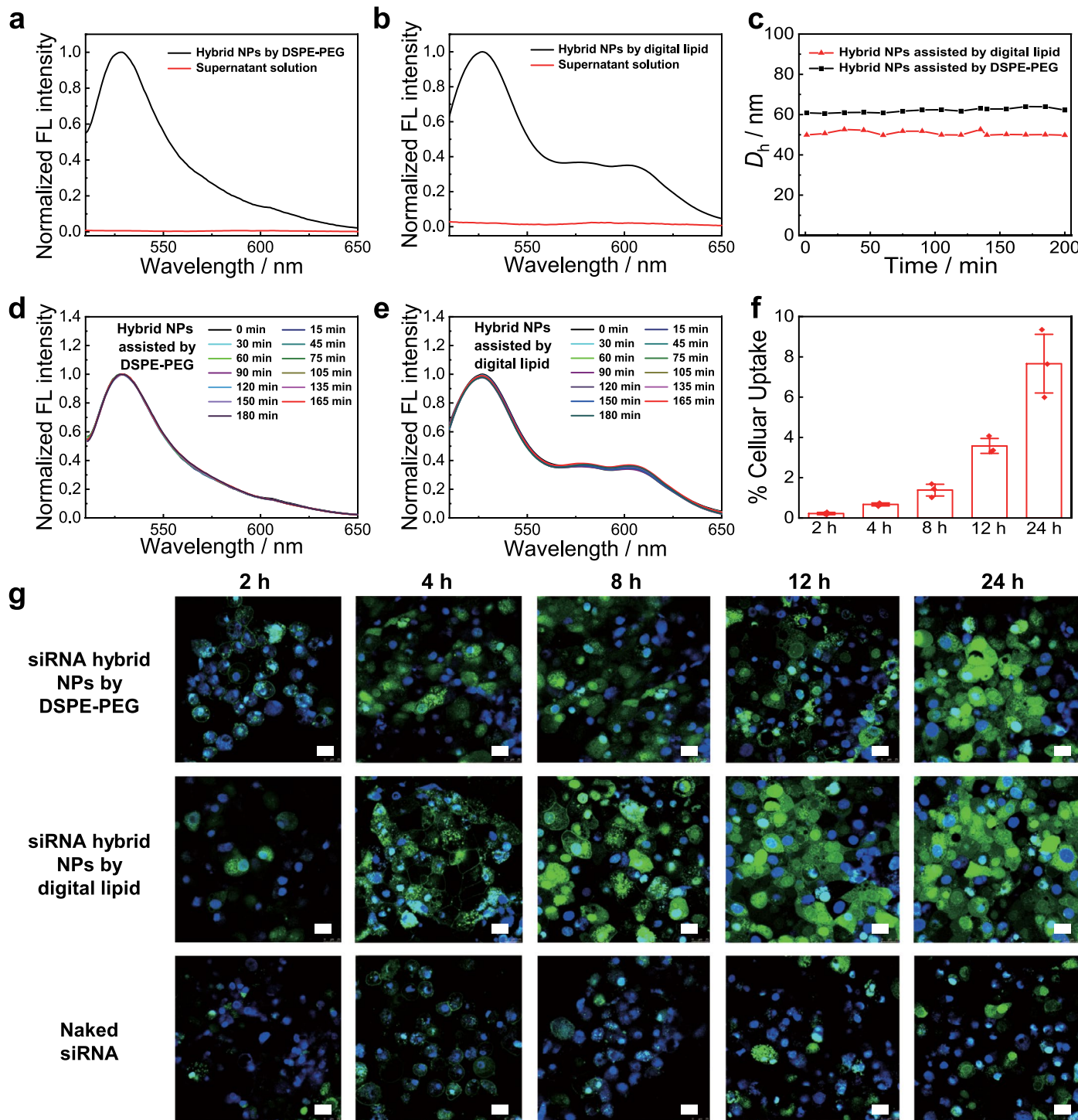


Extended Data Fig. 3 | Comparison of MALDI detection sensitivities for encoded amphiphiles. **a,b**, S/N values in MALDI characterization of T-00000000-dPEG and T-11111111-dPEG, and MALDI samples were prepared from unimer (THF solution) and micellar state (aqueous dispersion) at varying concentrations ($n = 3$ independent experiments; data are presented as mean values \pm SEM). **c,d**, MALDI-TOF mass spectra recorded for T-00000000-dPEG and T-11111111-dPEG; MALDI samples were prepared from unimer (THF solution)

and micellar state (aqueous dispersion) at $0.5 \mu\text{g}/\text{mL}$ and $1.0 \mu\text{g}/\text{mL}$, respectively. **e,f**, MALDI-TOF mass spectra recorded for T-000000-dPEG in the unimer state (THF solution) and (b) micellar state (aqueous dispersion) after coating onto rat spleen tissue slices and applying with DCTB/ CF_3COONa MALDI matrix. The negligible MS peak area difference indicated that encoded amphiphiles in the micellar NP state could be detected by MALDI with the sensitivity compared to those in the molecularly dissolved state.

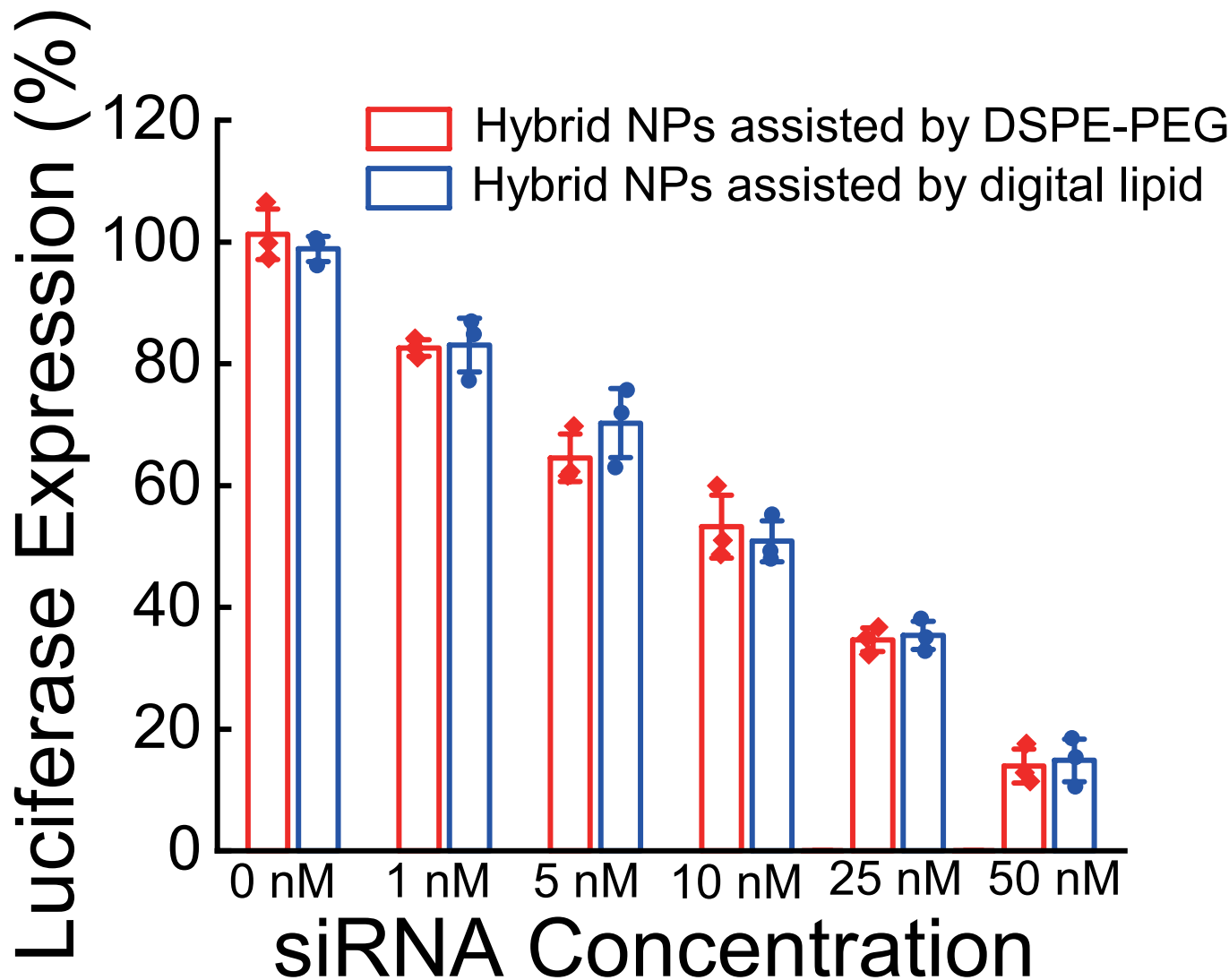


Extended Data Fig. 4 | Characterization of cationic lipid/siRNA/polymer hybrid NPs. **a**, Schematics for the fabrication of cationic lipid/siRNA/polymer hybrid NPs assisted by the digital lipid ($2C_{18}\text{-O}101\text{-OEG}_{16}\text{-OH}$). **b**, TEM image and **c**, dynamic laser scattering (DLS) results recorded for hybrid NPs stabilized by $2C_{18}\text{-O}101\text{-OEG}_{16}\text{-OH}$.

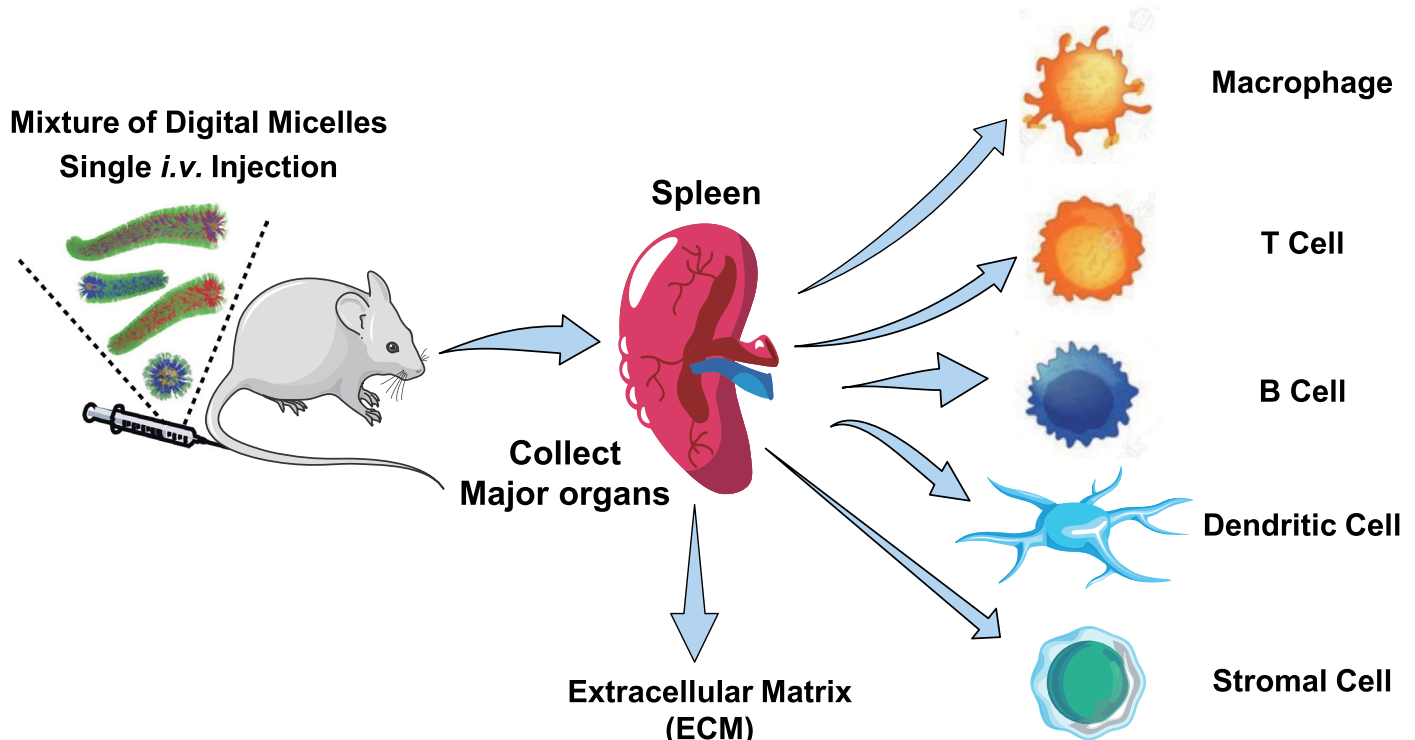


Extended Data Fig. 5 | Comparison of cationic lipid/siRNA/polymer hybrid NPs stabilized by digital lipid *versus* that by DSPE-PEG. **a,b**, Fluorescence emission spectra recorded for two types of FAM-siRNA-Luc hybrid NP dispersions and corresponding supernatant solutions after initially formed hybrid NPs were subjected ultrafiltration (MWCO, 100 kDa). **c**, Evolution of DLS sizes upon coincubation with 20% FBS. **d,e**, Evolution of emission intensities of two types of FAM-siRNA-Luc hybrid NPs upon co-incubation with 20% FBS. **f**, Uptake extents

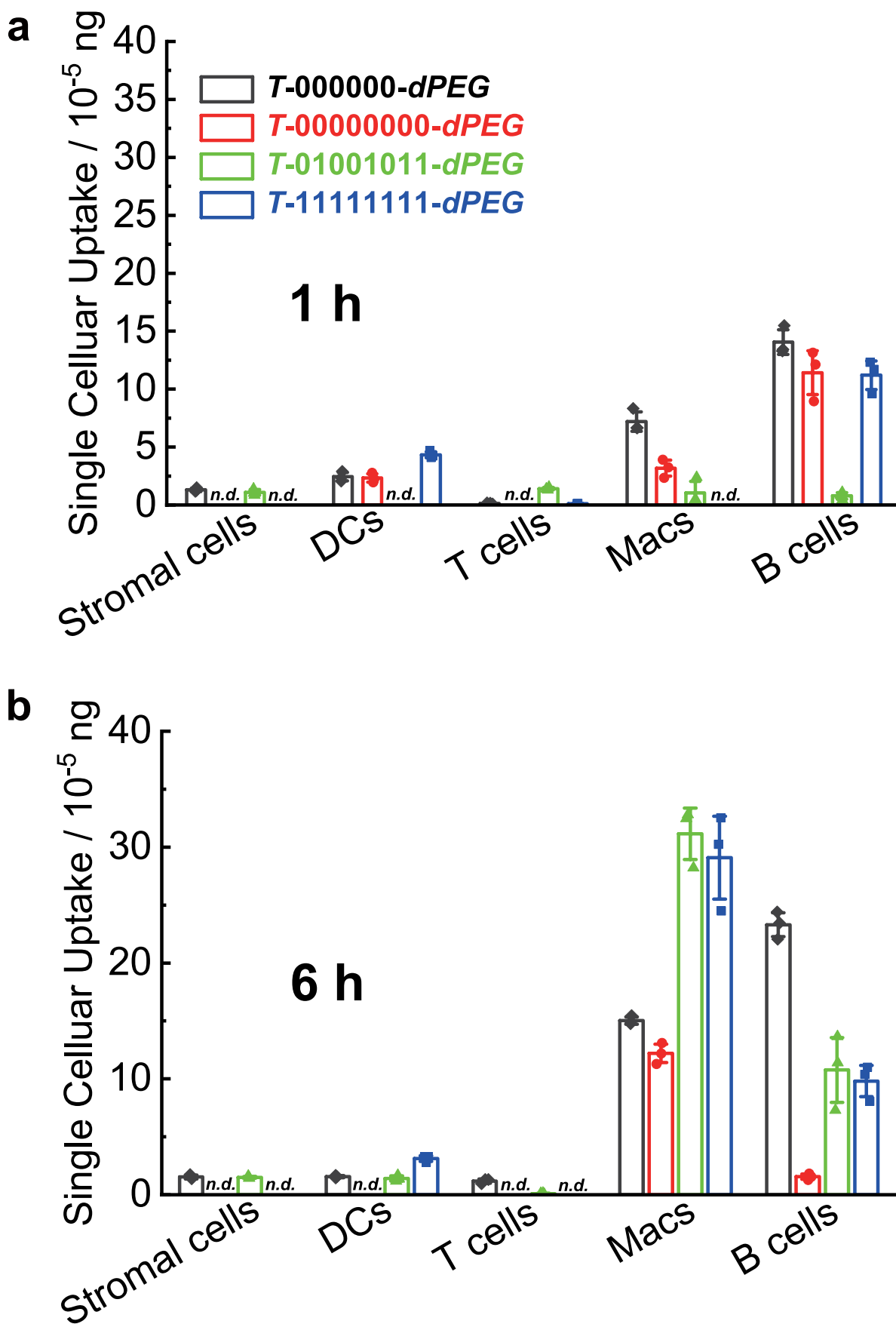
of FAM-siRNA-Luc hybrid NP stabilized by the digital lipid when co-incubated with BXPC-3 cells, as quantified by MALDI-TOF MS in a label-free manner ($n = 3$ biologically independent cells; data are presented as mean values \pm SEM). **g**, CLSM images (FAM channel) of BXPC-3 cells upon co-incubation with two types of FAM-siRNA-Luc hybrid NPs, whereas naked FAM-siRNA-Luc was used as a control. Scale bar: 25 μm .



Extended Data Fig. 6 | Biological behaviors of cationic lipid/siRNA/polymer hybrid NPs. Comparison of luciferase expression levels in Pan 02-Luc cells transfected with FAM-siRAN-Luc hybrid NPs stabilized by either DSPE-PEG or the digital lipid ($2C_{18}\text{-}0101\text{-}OEG_{16}\text{-}OH$) at varying siRNA concentrations ($n = 3$ biologically independent cells; data are presented as mean values \pm SEM).



Extended Data Fig. 7 | Cell sorting protocols for the spleen organ. Schematics of the sorting of immune cells (macrophages, T cells, B cells, and dendritic cells) and stromal cells from the spleen organ of BABL/c mice.



Extended Data Fig. 8 | Quantification of cellular uptake extents. Average absolute endocytosis mass of four types of encoded amphiphiles internalized by single stromal cell and each type immune cells (macrophage, T cell, B cell, and dendritic cell), which were sorted from the spleen organ of BABL/c mice

sacrificed at **a**, 1 h and **b**, 6 h post *i.v.* injection of a mixture of four types of digital micelles (21 nm nanospheres and 45 nm, 78 nm, and 245 nm nanorods; 11.2 mg/mL in total, 2.8 mg/mL for each type). n.d.: not detected ($n = 3$ biologically independent animals; data are presented as mean values \pm SEM).

Corresponding author(s): Shiyoung Liu

Last updated by author(s): June 03 2022

Reporting Summary

Nature Portfolio wishes to improve the reproducibility of the work that we publish. This form provides structure for consistency and transparency in reporting. For further information on Nature Portfolio policies, see our [Editorial Policies](#) and the [Editorial Policy Checklist](#).

Statistics

For all statistical analyses, confirm that the following items are present in the figure legend, table legend, main text, or Methods section.

n/a Confirmed

- The exact sample size (n) for each experimental group/condition, given as a discrete number and unit of measurement
- A statement on whether measurements were taken from distinct samples or whether the same sample was measured repeatedly
- The statistical test(s) used AND whether they are one- or two-sided
Only common tests should be described solely by name; describe more complex techniques in the Methods section.
- A description of all covariates tested
- A description of any assumptions or corrections, such as tests of normality and adjustment for multiple comparisons
- A full description of the statistical parameters including central tendency (e.g. means) or other basic estimates (e.g. regression coefficient) AND variation (e.g. standard deviation) or associated estimates of uncertainty (e.g. confidence intervals)
- For null hypothesis testing, the test statistic (e.g. F , t , r) with confidence intervals, effect sizes, degrees of freedom and P value noted
Give P values as exact values whenever suitable.
- For Bayesian analysis, information on the choice of priors and Markov chain Monte Carlo settings
- For hierarchical and complex designs, identification of the appropriate level for tests and full reporting of outcomes
- Estimates of effect sizes (e.g. Cohen's d , Pearson's r), indicating how they were calculated

Our web collection on [statistics for biologists](#) contains articles on many of the points above.

Software and code

Policy information about [availability of computer code](#)

Data collection

Bruker AVANCE III NMR 400 MHz spectrometer was used to acquire nuclear magnetic resonance (NMR) spectra of all synthetic samples
 Thermo Scientific LTQ Orbitrap mass spectrometer was used to acquired molecular mass and tandem mass spectra of synthetic samples
 Waters 1515 GPC was used to acquired molecular weight distributions
 Recycling preparative GPC (LABOACE LC-5060) was used to purify final products
 Autoflex Speed MALDI-TOF mass spectrometer (Bruker Daltonics, Germany) was used to acquire exact molecular weights and tandem MS spectra of sequence-defined samples
 Cryo-TEM was used to acquire morphology and size of nanostructures
 Gaussian 09 software was used for theoretical calculation and simulation
 Q200 different scanning calorimetry apparatus (TA instruments) was used for differential scanning calorimetry (DSC) measurements
 TA Discovery TGA instrument was used for thermogravimetric analysis
 Horiba spectrofluorometer was used for fluorescence measurement
 JEOL 2010 electron microscope was used to acquire morphology and size of nanostructures
 SAXS patterns were recorded at the synchrotron facility (SSRF, BL19U2 station, Shanghai, China) using monochromatic X-ray radiation
 Leica TCS SP5 microscope was used to acquire Confocal laser scanning microscopy (CLSM) images
 Multi-function microplate reader (Varioskan Flash) was used for chemiluminescence measurements
 Dolomite microfluidic nanoparticle generation system was used to fabricate barcoded micelles
 BD FACSaria™ III high sensitivity flow cytometer was used to sort immune cells and stromal cells from spleen organ of BALB/c mice
 Thermo Scientific Orbitrap Eclipse Tribrid mass spectrometer was used to quantify the absolute mass of digital micelles located within the extracellular matrix, and internalized by immune cells and stromal cells.

Data analysis

Origin 2019 was used to analyze mean, standard deviation, standard error and draw curves in relevant graphic figures

Data analysis

Imag-Pro Plus 6.0 was used to process imaging data
 FiberApp x32 was used to process cryo-TEM data
 FlexAnalysis 3.3 was used to process MALDI-TOF MS data
 Image-J 1.8.0 was used to calculate pixel intensities and Mander's tM1 parameters at the tissue slice levels.
 Gaussian 09 package was used to calculate bond dissociation energies of model molecules
 MestReNova 9.0.1 was used to analyze NMR data

For manuscripts utilizing custom algorithms or software that are central to the research but not yet described in published literature, software must be made available to editors and reviewers. We strongly encourage code deposition in a community repository (e.g. GitHub). See the Nature Portfolio [guidelines for submitting code & software](#) for further information.

Data

Policy information about [availability of data](#)

All manuscripts must include a [data availability statement](#). This statement should provide the following information, where applicable:

- Accession codes, unique identifiers, or web links for publicly available datasets
- A description of any restrictions on data availability
- For clinical datasets or third party data, please ensure that the statement adheres to our [policy](#)

The authors declare that all data supporting the findings of this study are available within the article, the associated source data and its Supporting Information and can also be obtained from the corresponding author upon reasonable request.

Human research participants

Policy information about [studies involving human research participants and Sex and Gender in Research](#).

Reporting on sex and gender

Use the terms sex (biological attribute) and gender (shaped by social and cultural circumstances) carefully in order to avoid confusing both terms. Indicate if findings apply to only one sex or gender; describe whether sex and gender were considered in study design whether sex and/or gender was determined based on self-reporting or assigned and methods used. Provide in the source data disaggregated sex and gender data where this information has been collected, and consent has been obtained for sharing of individual-level data; provide overall numbers in this Reporting Summary. Please state if this information has not been collected. Report sex- and gender-based analyses where performed, justify reasons for lack of sex- and gender-based analysis.

Population characteristics

Describe the covariate-relevant population characteristics of the human research participants (e.g. age, genotypic information, past and current diagnosis and treatment categories). If you filled out the behavioural & social sciences study design questions and have nothing to add here, write "See above."

Recruitment

Describe how participants were recruited. Outline any potential self-selection bias or other biases that may be present and how these are likely to impact results.

Ethics oversight

Identify the organization(s) that approved the study protocol.

Note that full information on the approval of the study protocol must also be provided in the manuscript.

Field-specific reporting

Please select the one below that is the best fit for your research. If you are not sure, read the appropriate sections before making your selection.

Life sciences

Behavioural & social sciences

Ecological, evolutionary & environmental sciences

For a reference copy of the document with all sections, see nature.com/documents/nr-reporting-summary-flat.pdf

Life sciences study design

All studies must disclose on these points even when the disclosure is negative.

Sample size

For in vitro experiments, 3 independent biological experiments were conducted in parallel. For in vivo experiments, 3 rats or mice were used in parallel for each experimental condition. No statistical methods were used to predetermine sample sizes.

Data exclusions

No data was excluded from the analysis.

Replication

The number of experimental repeats for individual assays were specified in figure legends. All attempts at replication were successful.

Randomization

SD rats and BALB/c mice were randomly distributed into each subgroup.

Blinding

The investigator who quantified nanoparticle contents in rat/mouse organs and blood proceeded without information of the injection and control group.

Investigator who characterize the morphologies of nanoparticles proceeded without information of the material composition and assembly process.

Reporting for specific materials, systems and methods

We require information from authors about some types of materials, experimental systems and methods used in many studies. Here, indicate whether each material, system or method listed is relevant to your study. If you are not sure if a list item applies to your research, read the appropriate section before selecting a response.

Materials & experimental systems

- | | |
|-------------------------------------|---|
| n/a | Involved in the study |
| <input type="checkbox"/> | <input checked="" type="checkbox"/> Antibodies |
| <input type="checkbox"/> | <input checked="" type="checkbox"/> Eukaryotic cell lines |
| <input checked="" type="checkbox"/> | <input type="checkbox"/> Palaeontology and archaeology |
| <input type="checkbox"/> | <input checked="" type="checkbox"/> Animals and other organisms |
| <input checked="" type="checkbox"/> | <input type="checkbox"/> Clinical data |
| <input checked="" type="checkbox"/> | <input type="checkbox"/> Dual use research of concern |

Methods

- | | |
|-------------------------------------|--|
| n/a | Involved in the study |
| <input checked="" type="checkbox"/> | <input type="checkbox"/> ChIP-seq |
| <input type="checkbox"/> | <input checked="" type="checkbox"/> Flow cytometry |
| <input checked="" type="checkbox"/> | <input type="checkbox"/> MRI-based neuroimaging |

Antibodies

Antibodies used

Antibodies used in this study have been listed as Supplementary Table 4. Dilution of each antibody used for immune cell sorting is 1:200.

Validation

All antibodies were well-recognized in the filed and have their validation statement on their manufactures' website:
 Anti-CD45 antibody: <https://www.bdbiosciences.com/en-us/products/reagents/flow-cytometry-reagents/research-reagents/single-color-antibodies-ruo/apc-cy-7-rat-anti-mouse-cd45.561037>
 Anti-CD3 antibody: <https://www.labome.com/product/Absin-Bioscience/abs180019.html>
 Anti-B220 antibody: <https://www.bdbiosciences.com/en-us/products/reagents/flow-cytometry-reagents/research-reagents/single-color-antibodies-ruo/bv510-rat-anti-mouse-b220-cd45r.563103>
 Anti-CD11b antibody: <https://www.bdbiosciences.com/en-us/products/reagents/flow-cytometry-reagents/research-reagents/single-color-antibodies-ruo/bv650-rat-anti-cd11b.563402>
 Anti-CD11c antibody: <https://www.bdbiosciences.com/en-us/products/reagents/flow-cytometry-reagents/research-reagents/single-color-antibodies-ruo/pe-cy-7-hamster-anti-mouse-cd11c.561022>
 Anti-CD80 antibody: <https://www.thermofisher.cn/cn/zh/antibody/product/CD80-B7-1-Antibody-clone-16-10A1-Monoclonal/12-0801-82>
 Anti-F4/80: <https://www.bdbiosciences.com/en-us/products/reagents/flow-cytometry-reagents/research-reagents/single-color-antibodies-ruo/pe-rat-anti-mouse-f4-80.565410>

Eukaryotic cell lines

Policy information about [cell lines and Sex and Gender in Research](#)

Cell line source(s)

3T3, 4T1, HepG2 cells were purchased from the Cell bank of the Chinese Academy of Science (Shanghai, China). LO2, BXPC-3-Luc and Pan O2-Luc cells were purchased from CELL RESEARCH company.

Authentication

None of the cell lines used in this study were authenticated by the authors.

Mycoplasma contamination

All cell lines were tested negative for mycoplasma contamination.

Commonly misidentified lines (See [ICLAC](#) register)

No misidentified cell line was involved in the study.

Animals and other research organisms

Policy information about [studies involving animals; ARRIVE guidelines](#) recommended for reporting animal research, and [Sex and Gender in Research](#)

Laboratory animals

All SD female rats (10 weeks) and BABL/c mice (5-6 weeks, female:male=1:1) were purchased from Experimental Animal Center of Anhui Medical University and all animal experiments were conducted following a protocol approved by Institutional Anhui Care and Use Committee (University of Science and Technology of China). All animals were maintained on a 12-12 light-dark cycle with a temperature of 23-25 °C and humidity of 48-52%.

Wild animals

No wild animals were used in the study.

Reporting on sex

SD female rats (10 weeks) and BABL/c mice (5-6 weeks, female:male=1:1) were used in this study.

Field-collected samples	<input type="checkbox"/> The study does not involve field-collected study.
Ethics oversight	<input type="checkbox"/> All animal experiments were conducted under protocols approved by Institutional animal Care and Use Committee of University of Science and Technology of China.

Note that full information on the approval of the study protocol must also be provided in the manuscript.

Flow Cytometry

Plots

Confirm that:

- The axis labels state the marker and fluorochrome used (e.g. CD4-FITC).
- The axis scales are clearly visible. Include numbers along axes only for bottom left plot of group (a 'group' is an analysis of identical markers).
- All plots are contour plots with outliers or pseudocolor plots.
- A numerical value for number of cells or percentage (with statistics) is provided.

Methodology

Sample preparation

The collected mice spleens were immediately placed in 5 mL PBS containing 1% FBS and 2 mM EDTA. After grounding, filtration, and washing with PBS containing 1% FBS and 2 mM EDTA, the suspension containing spleen cells and extracellular matrix was obtained. Erythrocytes were lysed and remaining cells were counted and adjusted to 1×10^6 cells/mL. The following antibodies were used for cell sorting: T cells (anti-CD45-APC, anti-CD3-PerCP Cy5.5), B cells (anti-CD45-APC, anti-B220/CD45R-BV510), DC cells (anti-CD11c-FITC, anti-CD80-PE), macrophages (anti-CD11b-BV650, anti-F4/80-PE), and spleen stromal cells (anti-CD45-). Spleen cells were sorted on a BD FACSAria III high sensitivity flow cytometer, affording stromal cells (5×10^5), CD45+ B220/CD45R+ (B cells, 5×10^5), CD45+ CD3+ (T cells, 15×10^5), CD11c+ CD80+ (DCs, 2×10^5), and CD11b+ F4/80+ (Macs, 2×10^5).

Instrument

BD FACSAria III high sensitivity flow cytometer.

Software

BD FACSAria III software and FlowJo 10 Mac software.

Cell population abundance

Purity of isolated samples was determined by antibody stain and flow cytometry. Sample purity was greater than 90%.

Gating strategy

For detailed gating representative plots, please refer to Supplementary Figs. 104–107. Positive signals were gated based on non-staining negative control.

For sorting B cells from mice spleen, cells were selected by excluding the debris according to FSC-H and SSC-H, followed by single cells using SSC-A and SSC-H. Whole B cell population were gated by selecting CD45+B220/CD45R+ cells (Supplementary Fig. 104).

For sorting T cells from mice spleen, cells were selected by excluding the debris according to FSC-H and SSC-H, followed by single cells using SSC-A and SSC-H. Whole T cell population were gated by selecting CD45+CD3+ cells (Supplementary Fig. 105).

For sorting dendritic cells from mice spleen, cells were selected by excluding the debris according to FSC-H and SSC-H, followed by single cells using SSC-A and SSC-H. Whole dendritic cell population were gated by selecting CD11c+CD80+ cells (Supplementary Fig. 106).

For sorting macrophages from mice spleen, cells were selected by excluding the debris according to FSC-H and SSC-H, followed by single cells using SSC-A and SSC-H. Whole macrophage population were gated by selecting CD11b+F4/80+ cells (Supplementary Fig. 107).

Tick this box to confirm that a figure exemplifying the gating strategy is provided in the Supplementary Information.